Korean J. Chem. Eng., 37(2), 274-289 (2020)
DOI: 10.1007/s11814-019-0435-3

pISSN: 0256-1115
eISSN: 1975-7220

Bio-extract assisted in-situ green synthesis of Ag-RGO nanocomposite film for enhanced naproxen removal

Somen Mondal†, Surabhi Patel, and Subrata Kumar Majumder†

Department of Chemical Engineering, Indian Institute of Technology Guwahati, Guwahati 781039, India
(*Received 2 October 2019 • accepted 19 November 2019*)

Abstract−The present study reports in-situ green synthesis of Ag-RGO nanocomposite film using turnip leaves-extract as a reducing as well as a capping agent and its application as a highly efficient naproxen adsorbent from a contaminated aqueous solution. The nanocomposite was characterized employing XRD, Raman and FT-IR spectroscopy, FETEM and FESEM microscopy, EDS spectroscopy. The pseudo-second-order and Elovich kinetic model furnished the best correlation of the experimental data, specifying the adsorption as the rate-limiting step for naproxen (NPX) removal by Ag-RGO composite film. The Freundlich and Dubinin-Radushkevich (D-R) isotherms represented the experimental adsorption data satisfactorily, suggesting a multilayered chemical adsorption process on the heterogeneous adsorbent surfaces. The process parameters were optimized to get the maximum adsorption capacity, which was obtained as 229.25 mg g^{-1} (92.62%). The parametric effects of pHs and NPX concentrations were tested within a range of 2.50-8.50 and 25-100 mg dm^{-3}, respectively, for the contact time of 0.33-3 min at a constant temperature (298 K) and adsorbent dose (20.2 mg). The feasibility of the regeneration of the materials after adsorption is based on the experimental results. The experimentally optimized process parameters were validated using response surface methodology (RSM).

Keywords: Ag-RGO Nanocomposite, Green Synthesis, Naproxen Removal, Adsorption Kinetics and Isotherms, Process Optimization

INTRODUCTION

Naproxen ($C_{14}H_{14}O_3$, NPX), is a widespread, non-steroidal anti-inflammatory drug, widely prescribed for pain relief such as muscle aches, headache, dental pain, tendonitis, and menstrual cramps. After intake, drugs are absorbed and take part in metabolic reactions. The organisms leave the unmetabolized substances comprising these drugs via urine or sludge into the sewage water. Moreover, the main sources of these drug contaminations are the inefficient effluent of the pharmaceutical industries, the improper ejection of unused or expired drugs in hospitals, which are increasing water contamination day by day due to their stability. Naproxen may affect water quality adversely. Human life and ecosystem can be directly influenced by the long-term intake of contaminated aquatic food like fish and potable water [1,2]. It may affect the regulation and functioning of the organisms present in the ecosystems by influencing the activity of enzymes as it is a biologically active substance [3]. The reported range of their existence in the environment is 0.1-2.6 μg dm^{-3} in treated wastewater and 0.01-0.1 μg dm^{-3} in surface waters [1,7,15]. Researchers have employed various removal methods for the separation or degradation of NPX from contaminated water. Coagulation-flocculation, sedimentation, ultrasonic-degradation processes are not effective enough [4]. Other important processes are photo-degradation [5], bio-degradation [3,6] and advanced oxidation processes such as chlorination [7], UV/H_2O_2 [8,9], ozone (O_3) [10,11] and their combinations or others. Advanced oxidation processes may produce 1-(6-methoxy-2-naphthyl) ethanol, 1-(6-methoxynaphthalen-2-yl) ethanone, 2-ethyl-6-methoxynaphthalene, 1-(6-methoxynaphthalen-2-yl) ethyl-hydroxy-peroxide as the byproducts in the reaction medium [5]. Although the advanced oxidation processes are highly effective to remove or degrade naproxen from the aqueous medium, they may create environmental toxicity due to the production of highly toxic intermediates than the parent compound [12]. However, the adsorption process is quite effective and mostly used for the removal of naproxen without the formation of any harmful byproducts. Activated carbon [2,13], activated carbon nanocomposite [14], activated sludge [15], micelle-clay complex [16], nanoparticles decorated onto graphene oxide [17] are used as adsorbents extensively.

In recent years, reduced graphene oxide (RGO) has been attracted great attention for its good electrical, thermal, mechanical, and optical properties. Moreover, RGO and its nanocomposites are broadly used as excellent adsorbents and applied in water purification processes. Adsorption being a surface phenomenon not only depends on the surface area and micropores present, but it also on the surface characteristics of the adsorbing materials. The 2D planes of RGO film with the attachment of fewer amounts of functional groups provide high surface area and bonding sites susceptible to adsorption. The delocalized π-electrons present in RGO film have strong binding efficiency towards the harmful pollutants, which makes it a rapid adsorbent for the removal of pollutants [18]. Otherwise, nanoparticles have efficient disinfectant or degradation or complex formation ability depending on the surface charge under optimized pH condition. Hence, the nanoparticle decorated RGO film may

†To whom correspondence should be addressed.
E-mail: skmaju@iitg.ac.in, somen.mondal@iitg.ac.in

provide excellent removal efficiency towards various water pollutants like harmful organic dyes [19-21], heavy metals [21-24], phenol, and phenolic compounds [21,23] as well as pharmaceuticals [25,26].

Previously, RGO and its composites, were produced using a variety of reducing agents like acids such as alanine [27] and ascorbic acid [28], metal or metal oxides [29,30], reducing sugars [31], reducing salts [32], hydrazine [33,34], organic compounds like indole [35] and plant extracts [36-38]. These RGO were utilized for versatile purposes other than the removal of naproxen. Very few studies have been performed for the adsorption of NPX on RGO or RGO nanocomposites, produced by the chemical reduction using sodium borohydride [39] and sodium ascorbate [40]. Moreover silver-decorated reduced graphene oxide nanocomposites have attracted the attention of the researchers for their huge application fields like heterogeneous nanocatalysis [41,42], hydrogen peroxide detection [43], photocatalysis [44,45], temperature [46], ammonia gas [47] and H_2S gas sensors [48] and also in water purification [49,50].

Nowadays the use of bio-extracts as the reducing agents is gaining importance in the scientific community for the green synthesis of nano-particles that are useful for their various kinds of applications as said earlier. In this regard, turnip (Brassica rapa subsp. Rapa) leaves-extract is remarkable [51-53]. The phenolic and nitrogen compounds, vitamins, reducing sugars, terpenoids, and other metabolites present in the turnip leaves may act as the reducing agents in green synthesis of nanoparticles [51]. The presence of polyols, hydroxyl and carboxylic groups may act as reducing as well as a capping agent in the nanoparticle synthesis [52]. Turnip leaves-extract contains a sufficient amount of ascorbic acid or vitamin C (95.28±0.98 to 143.38±7.31 mg per 100 g) and total phenolics (218.54±48.77 to 240.01±6.08 mg per 100 g) may signify it as an effective reducing medium [53]. The practical application of the Ag-RGO nano-composite in the water purification fields should be advantageous for its higher adsorptive removal capacity and efficiency towards water contaminants, as RGO itself is a good adsorbent [40]. The conductive Ag-nanoparticles in the synthesized material may have antimicrobial activity [54] based on the charge generated on it depending on the experimental pH values [55]; and it can show catalytic activity towards naproxen degradation/complex formation [56]. The Ag-nanoparticles degraded byproducts formed, if any, may also be adsorbed/removed by the RGO surfaces with the higher π-π interactions. Ag-nanoparticles may also increase the hydrophilicity of the graphene film. Higher hydrophobicity can provide a higher adsorption capacity by expanding the adsorbate and adsorbent interactions. Hence, the prepared Ag-RGO film may be utilized for the adsorptive removal of naproxen without any harmful byproduct generation.

To the best of the authors' knowledge, the use of the silver (Ag) nanoparticles decorated RGO (Ag-RGO) film synthesized by the green method using turnip leaves-extract is the initiation for the adsorptive removal of naproxen, which is considered in the present study. The main objectives of the present study were to synthesize the Ag-RGO film using turnip leaves-extract and its utilization as efficient remediation of naproxen by adsorption from the naproxen-contaminated water without the formation of harmful by-products. Moreover, the adsorption parameters were optimized to obtain the maximum adsorption capacity. The adsorption kinetics and equilibrium isotherms were also based on the present experimental conditions.

EXPERIMENTAL

1. Reagents and Materials

Natural graphite flakes (atomic weight=12.01, assay≥99.5%) and caustic soda pellets (NaOH, MW=40.00, assay=98.0%) were bought from Himedia Laboratories Private Ltd. Potassium permanganate ($KMnO_4$, MW=158.03, assay=99.0%) was purchased from Central Drug House (P) Limited. The other required chemicals, 98.0% sulfuric acid (H_2SO_4, MW=98.08 g mol^{-1}, assay=95.0-98.0%), 88.0% phosphoric acid (H_3PO_4, MW=98.0 g mol^{-1}, assay≥85.0%), 37.0% hydrochloric acid (HCl, MW=36.46 g mol^{-1}, assay=36.5-38.0%), 30.0% hydrogen peroxide (H_2O_2, MW=34.01 g mol^{-1}, assay=29.0-32.0%) and silver nitrate ($AgNO_3$, MW=169.87 g mol^{-1}, assay≥99.5%) of ACS reagent grade were supplied by Merck Life Science Private Ltd. Hayman Group Limited supplied ethyl alcohol AR (C_2H_6O, MW=46.07 g mol^{-1}, assay=99.9%). Anhydrous naproxen ($C_{14}H_{13}O_3$, MW=230.26 g mol^{-1}, assay=98.5-101.5%) meets USP testing specifications supplied by Sigma-Aldrich (USA), was used in the present experiments without any further purification. Milli-Q water was obtained from the Millipore synthesis unit (Model: Elix-3, Milli-Q; Make: Millipore, USA) present at the analytical laboratory, IIT Guwahati.

2. Preparation of Graphene Oxide (GO)

GO was prepared following the improved Hummers method without using $NaNO_3$, which restricts the release of NO_X. The GO produced by this method constitutes a more regular structure with the less disrupt basal plane, making the process advantageous for mass production [57]. Improved Hummers method is further modified herewith (modified improved Hummers method), to produce high quality GO in a more economical way of consuming lesser time and chemicals than the improved Hummers method. 90 cm^3 concentrated H_2SO_4 and 10 cm^3 concentrated H_3PO_4 acids (9 : 1 ratio) were mixed and stirred for 30 min using a magnetic stirrer. Then 2 g of natural graphite flakes (GF) were added to the acid mixture and stirred for 1 h. The mixture temperature was maintained at 273-278 K with the help of an ice bath and 12 g of $KMnO_4$ was added slowly with continuous stirring. The mixture was stirred for 90 min, followed by sonication for 1 h at 208 K and 20 min at 358-363 K, respectively. A deep green color solution was obtained, indicating the completion of the oxidizing reaction. Then 150 cm^3 and 350 cm^3 of milli-Q water were added successively and sonicated the solutions for 1 h, respectively, at 298-308 K to complete the hydrolysis. A brown color mixture was obtained and 10 cm^3 30.0% H_2O_2 was added to the brown color solution with 10 min continuous stirring to remove the unreacted $KMnO_4$ from the solution mixture, then the brown color solution turned ito yellow. The prepared GO was washed with 1.5 dm^3 of 1 : 10 aqueous HCl solution (direct dilution of 37.0% concentrated HCl) to remove metal ions. The prepared GO was washed and centrifuged (12,000 rpm for 20 min) with the milli-Q water several times (minimum seven times) resulting in GO hydrogel of final pH 3.02. The prepared GO

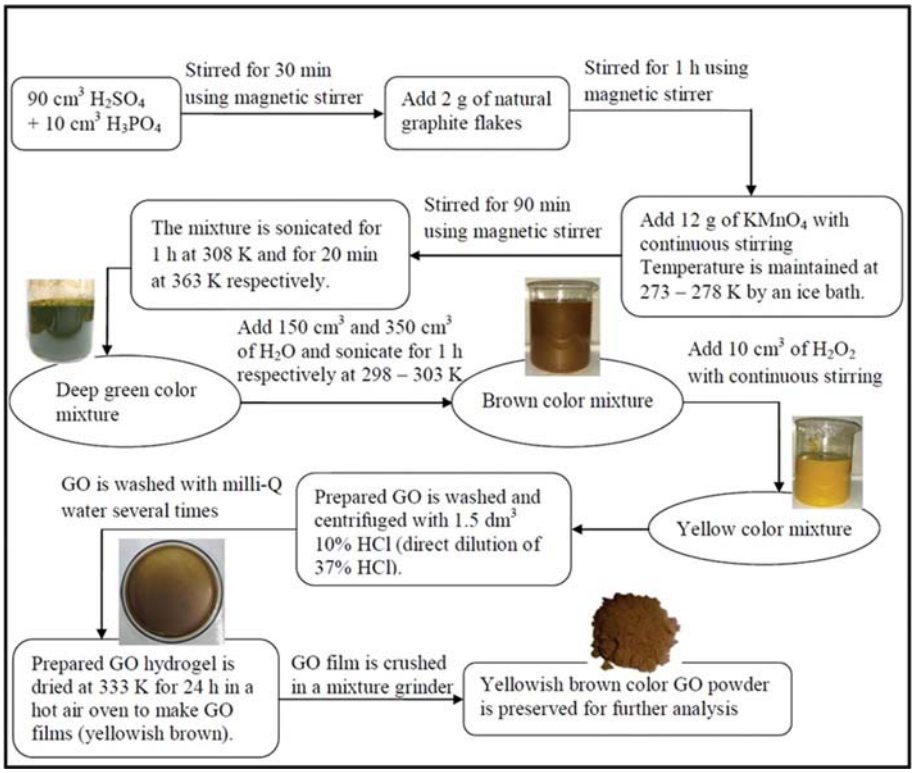

Fig. 1. GO preparation scheme (modified improved Hummers method).

hydrogel was then dried in a hot air oven for 24 h at 373 K. The dried GO film was crushed by a mixture grinder to get GO powder of yellowish-brown color, which was preserved for the further analysis. A detailed flow diagram for the GO synthesis is shown in Fig. 1.

3. Green Synthesis of Silver-reduced Graphene Oxide (Ag-RGO) Nanocomposite

100 g of fresh green turnip leaves collected from the local market was cut into pieces and taken into 400 cm^3 milli-Q water in a one dm^3 glass beaker. It was heated at 353 K for 2 h with continuous stirring and filtered to get the leaves-extract. The leaves-extract was then concentrated to 100 cm^3 by boiling (yellowish-green in color) and preserved for further use (pH 5.30). After that, 100 mg of GO powder was dispersed into 50 cm^3 milli-Q water by 1 h sonication at room temperature 298 K (pH 2.96). Then 20 cm^3 0.1 M $AgNO_3$ (pH 9.86) solution and 70 cm^3 concentrated turnip leaves-extract were added into the GO suspension. The mixture was then heated for 24 h at 353-363 K temperature with continuous stirring (pH 5.92). The color of the solution turned black with the simultaneous reduction of GO to RGO and Ag^+ to Ag-nanoparticles. The prepared RGO film decorated with Ag-nanoparticles (Ag-RGO nanocomposite film) was filtered and centrifuged with milli-Q water (13,400 rpm for 20 min), dried at 363 K for 24 h in an oven and conserved for the additional experimentation.

4. Methods

The physical properties and structure of the nanocomposite material were analyzed by X-ray powder diffraction (XRD) (Model: D8 Advance, Make: Bruker, Netherlands) with Cu-Kα radiation of wavelength 1.5406 Å (40 kV, 40 mA) over the range of 2θ=10-80° at a rate of 3° min^{-1}. The surface functional groups of the synthesized material were recognized by Fourier-transform infrared spectroscopy (FTIR) (Model: IR Affinity-1, Make: Shimadzu, Japan) using finely ground KBr with 0.5% of the sample to form pellets with the average of 30 scans ranges from 400-4,000 cm^{-1}. The graphene layer formed in the prepared sample was analyzed by a Raman system (Make: Horiba Jobin Vyon, Model: LabRam HR, Japan) with the help of the band shift by dispersion of monochromatic light (wavelength 488 nm). Field emission transmission electron microscope (FETEM) (Make: JEOL, Model: 2100F, Japan) and Field emission scanning electron microscope (FESEM) (Make: Zeiss, Model: Sigma, Germany) were used to inspect the surface morphology of the prepared sample. The composition of the prepared material was analyzed by energy-dispersive X-ray spectroscopy (EDS). NPX concentrations before and after the adsorption experiments were measured by high-performance liquid chromatography (HPLC) (Model: Prominence HPLC System; Make: Shimadzu, Singapore). The other necessary instruments, like the digital balance (Model: ME 204, Make: Mettler Toledo, Switzerland), pH meter (Model: pH 700, Make: Eutech Instruments, Singapore), magnetic stirrer with hot plate (Make: Antech, Model: AN-MSH-680), ice flaker machine (Make: NTF, Model: SLF 225, Italy), sonicator (Model: 3.5 L/00H/DTC, Make: PCI, India), centrifuge (Model: 2-16P, Make: Sigma, Germany), hot air oven (Model: Digital, Make: SoNuu, India) and mixture grinder (Model: LLMG20 500 W, Make: Lifelong, India) were used for the desired material synthesis purpose.

5. Adsorption Experiments

Naproxen adsorption was conducted in a batch mode with continuous stirring with magnetic stirrer using 20.2 mg of Ag-RGO

composite (suspended by 1 h sonication in 2 cm^3 milli-Q water) and 50 cm^3 NPX solutions in each case. Continuous mixing was achieved by moving a glass rod in the opposite direction of magnetic stirring. The effective parameters like pH (2.50, 4.50, 6.50 and 8.50 at room temperature 298 K), adsorption time (0.33-3.0 min) and naproxen concentration (25-100 mg dm^3) on the adsorption capacity were investigated. The naproxen removal percentages (R%), the adsorption capacities (mg g^{-1}) at equilibrium and at time t were calculated based on the naproxen concentrations before and after the adsorption studies following Eq. (1), Eq. (2) and Eq. (3) respectively.

$$\%R = \frac{C_0 - C_e}{C_0} \times 100 \quad (1)$$

$$q_e = \frac{V}{m}(C_0 - C_e) \quad (2)$$

$$q_t = \frac{V}{m}(C_0 - C_t) \quad (3)$$

where C_0 (mg dm^{-3}) and C_e (mg dm^{-3}) are the initial and equilibrium concentrations of naproxen in solution, q_e (mg g^{-1}) is the equilibrium adsorption capacity, C_t (mg dm^{-3}) and q_t (mg g^{-1}) are the concentration of NPX in the solution and adsorption capacity of the adsorbent at time t. V (dm^3) is the volume of naproxen solution taken for each batch adsorption study and m (g) is the adsorbent (Ag-RGO) dosage.

The concentration of NPX was measured by HPLC, provided with a UV detector and a C18 column (Eclipse XDB, Agilent, USA) having dimensions of 250 mm×4.6 mm, and packed with the particles of 5 μm diameter. The mobile phase was a mixture of acetonitrile (50%) and 1% aqueous solution of acetic acid (50%) with an isocratic flow rate of 1.0 cm^3 min^{-1}. The detection wavelength

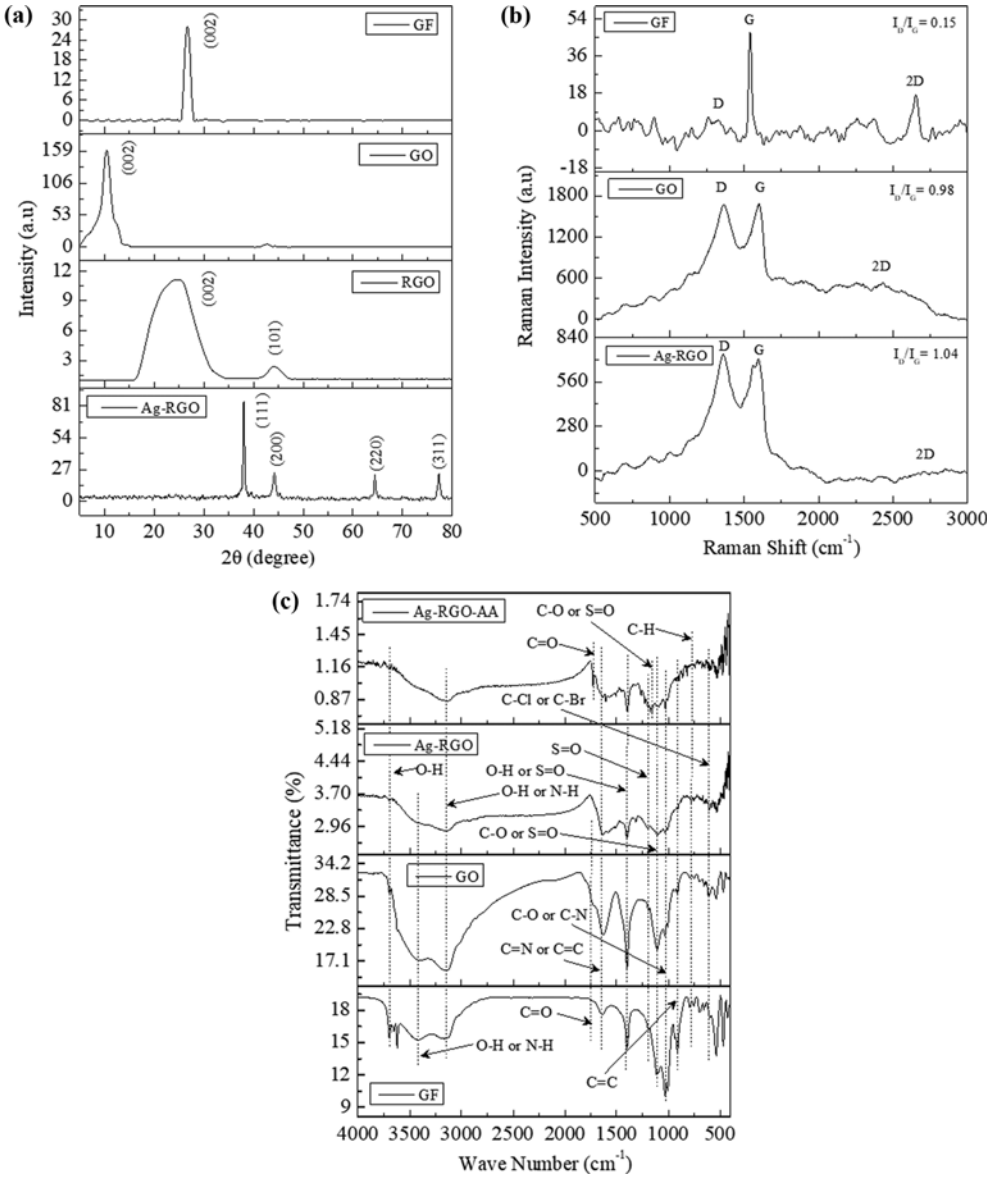

Fig. 2. (a) X-ray diffraction pattern (b) Raman spectroscopy of GF, GO, Ag-RGO nanocomposite and (c) FTIR spectrum of GF, GO, Ag-RGO nanocomposite and Ag-RGO-AA (Ag-RGO nanocomposite after adsorption).

and temperature were set at 260 nm and 298 K, respectively.

6. Adsorbent Regeneration Experiments

Regeneration study is a crucial factor for the industrial use of adsorbents. The used adsorbent was regenerated at room temperature by mixing with 100 cm^3 pure ethyl alcohol. The mixture was stirred for 1 h using magnetic stirrer, sonicated for 30 min, filtered, washed with ethyl alcohol, and finally dried in a hot air oven for further use. The similar process was repeated for regeneration purposes up to the fifth recycle.

RESULTS AND DISCUSSION

1. Material Characterization

Fig. 2(a) shows the X-ray diffraction patterns for GF, GO, RGO, and Ag-RGO. GF shows the sharp peak at 2θ=26.6°, which corresponds to interlaying spacing value (d_s) of 3.36 Å for (002) plane. GO has the much higher d spacing value (28.0 Å) for 2θ=10.45° due to the involvement of oxide bonds, which confirms the extensive oxidation of GF. The pattern for Ag-RGO shows the four peaks 38.1°, 44.2°, 64.4°, and 77.4° and assigned planes were found to be (111), (200), (220), and (311) [46,58-62]. This approves face-centered cubic (FCC) lattice in Ag-RGO [JCPDS no. 01-087-0597].

Raman spectroscopy is one of the widely used and most sensitive techniques to characterize disorder in sp^2 hybridized carbon materials. Comparison of Raman spectra of GF, GO, and Ag-RGO is shown in Fig. 2(b). The plane stretching vibrations between sp^2 carbon atoms are responsible for G band (graphitic peak) due to the E_{2g} vibrational mode resulted from the C-C bond stretching inside all the sp^2 carbon samples, whereas the D band (disorder peak) is important for the A_{1g} vibrational mode arising from the disordered shape of sp^2-hybridized carbon systems. GF shows the G band characteristic peak at 1,540 cm^{-1} as well as a weaker D band at 1,330 cm^{-1}. In GO, G band widened and shifted towards 1,540 cm^{-1} to 1,600 cm^{-1} due to amorphization in the lattice [58,59,61]. Higher I_D/I_G of GO (0.98) than GF (0.15) indicates the oxidation. In Ag-RGO the I_D/I_G increased from 0.98 to 1.04, which may correspond to a higher degree of disorder, new and isolated smaller graphitic domains or multilayer formation due to chemical bonding between GO and Ag-nanoparticles [58,60].

Fig. 2(c) shows the FTIR spectrum of GF, GO, Ag-RGO, and Ag-RGO-AA (Ag-RGO after adsorption study), which determines the functional groups present in the materials. Peaks at 3,695 cm^{-1}, 3,422 cm^{-1}, and 3,151 cm^{-1} correspond to the O-H bond stretching of free or intra-molecularly bonded alcohol. The peak at 1,394 cm^{-1} represents O-H bending of alcohol or carboxylic acid groups. Peaks at 3,422 cm^{-1}, and 3,151 cm^{-1} demonstrate the presence of N-H bonds stretching of primary amines or amine salts. The peak at 1,646 cm^{-1} represents medium or strong C=C stretching of mono-substituted, di-substituted or conjugated alkene groups, whereas the peak at 914 cm^{-1} corresponds to the C=C bending of alkene groups. The wavelength 1,646 cm^{-1} represents the common C=N bond stretching of imine or oxime groups. The peaks at 1,394 cm^{-1} and 1,198 cm^{-1} are evidence of S=O bonds stretching of sulfate or sulfonyl chloride. The evidence of strong bond stretching of C-O secondary alcohol, a tertiary alcohol, aliphatic ether, vinyl ether or alkyl aryl ether, was confirmed by the peaks at 1,198 cm^{-1}, 1,109 cm^{-1}, and 1,023 cm^{-1}. The peak at 1,023 cm^{-1} also corresponds to the presence of common C-N bond stretching of amine groups. The peak identified at 773 cm^{-1} is the evidence of C-H bending of the mono-substituted and 1-2-disubstituted benzene derivative. The peak at 609 cm^{-1} represents the bond stretching of the halo compounds (C-Cl or C-Br). The peak present in Ag-RGO-AA compound at the wavelength 1,721 cm^{-1} corresponds to the C-H bending of aromatic compounds or C=O stretching of aldehydes, conjugated anhydrides, aliphatic ketones, carboxylic acids or α,β-unsaturated esters. Strong C-O bond stretching of tertiary alcohol or the S=O bond

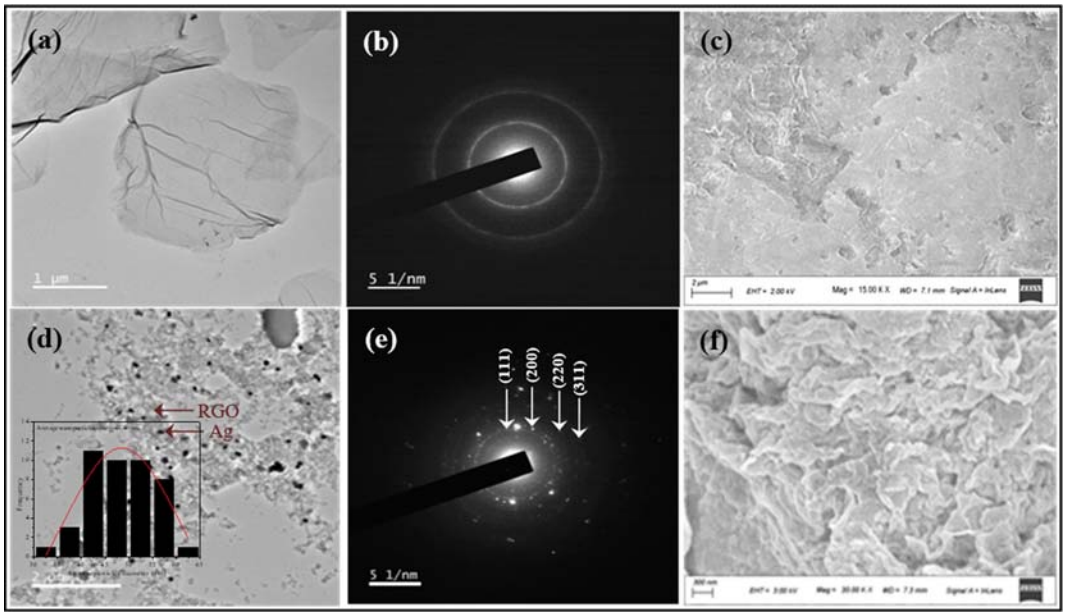

Fig. 3. (a) FETEM micrograph of GO, (b) SEAD pattern of GO, (c) FESEM image of GO, (d) FETEM micrograph of Ag-RGO and size distribution of Ag-nanoparticles (inset figure), (e) SEAD pattern of Ag-RGO and (f) FESEM image of Ag-RGO.

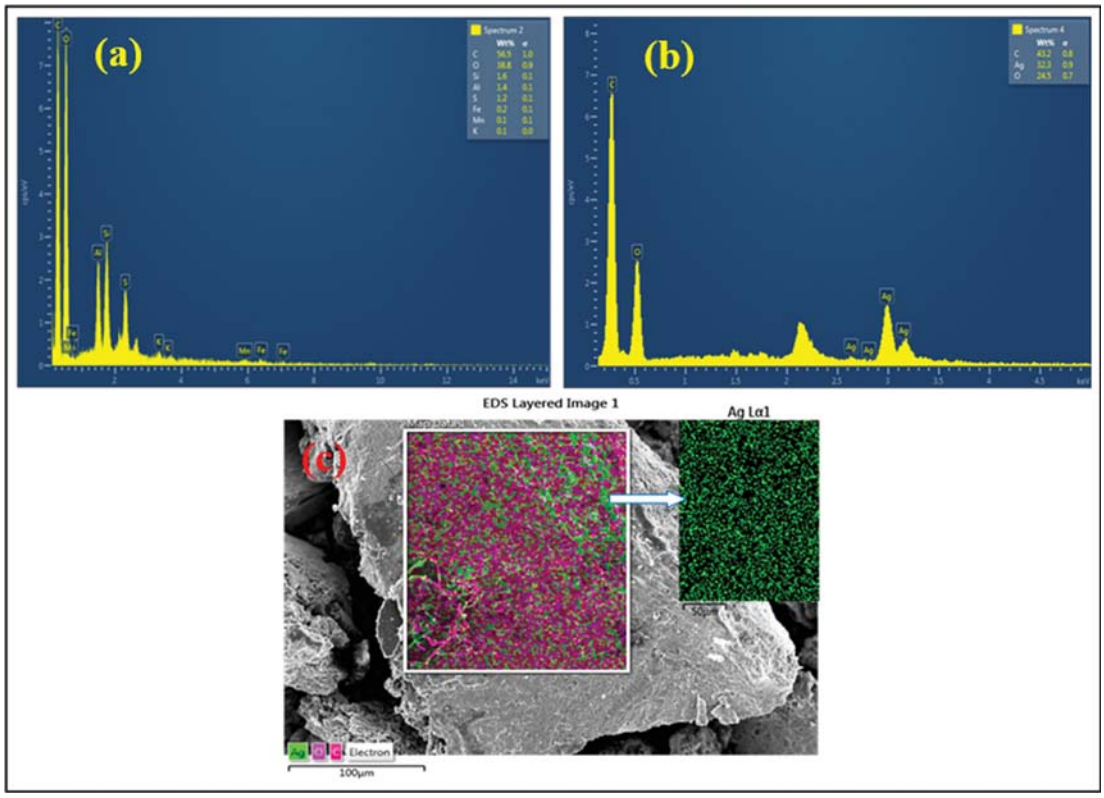

Fig. 4. (a) EDS spectrum of GO, (b) EDS spectrum of Ag-RGO and (c) EDS mapping of Ag-RGO nanocomposite.

stretching of sulfonamides, sulfones or sulfonic acids were represented by the peak at 1,155 cm^{-1} [58,60,61,63,83]. The FTIR spectrum of Ag-RGO (before adsorption) and Ag-RGO-AA (after adsorption) indicates a decrease in the intensity of the peaks for the latter one along with some shifts or changes in some of the characteristic bands. In case of Ag-RGO-AA, the peaks disappeared at 1,307 cm^{-1} and appeared at 1,721 cm^{-1}, 1,264 cm^{-1}, 859 cm^{-1}, 816 cm^{-1}. The peak of C-O shifted from 1,109 cm^{-1} to 1,155 cm^{-1}. These results imply the possibility that adsorption may take place through an ion-exchange process rather than complexation [63,64]. Figs. 3(a) and 3(d) show the FETEM micrographs of GO and Ag-RGO. The images illustrate the sheet-like structures and homogeneous dispersion of GO and Ag-nanoparticles on the RGO sheets, respectively. Ag-nanoparticles are found more or less uniform in shape and sizes (diameter: 34.49 nm to 61.70 nm) with an average particle diameter of 48.46 nm (inset figure of Fig. 3(d)). According to Meng et al. [65], the Ag-RGO nano-crystals with the Ag-particle (diameter of 40-45 nm) showed an efficient catalytic activity in 8 minutes, and according to Bastus et al. [56], the Ag-nanoparticles of diameter 53.2 nm functionalized more easily than 19.7 nm and 103.1 nm particles (53.2 nm>103.1 nm>19.7 nm) and also were stable enough against aggregation. Hence, high functionalization efficiency and catalytic activity, as well as naproxen degradation efficiency, may be provided by the newly synthesized Ag-RGO material without Ag-nanoparticles aggregation. Moreover, the larger size of the Ag-particles may be due to some aggregation bound by the bio-organic capping molecules present in the leaves-extract [62]. Fig. 3(c) and 3(f) demonstrate the FESEM images of GO and Ag-RGO, which illustrate the even distribution of Ag-nanoparticles on RGO sites associated with presence of oxygen-containing polar functional groups on RGO surface [59,66]. Fig. 3(b) and 3(e) represent the SEAD pattern for GO and Ag-RGO. The four rings were assigned to face-centered cubic lattice plane of Ag-nanoparticles which are (111), (200), (220) and (311).

Meanwhile, the ring-shaped pattern of diffraction recommends the crystalline structure of Ag-nanoparticles [66].

Fig. 4(a) and 4(b) represent the EDS spectrum of GO and Ag-RGO, respectively, which confirms the introduction of Ag-nanoparticles on RGO sheet. Fig. 4(a) validates the presence of carbon and oxygen in GO. It is evident in Fig. 4(b) that the relative intensity of C decreased in Ag-RGO, and Ag-nanoparticles are present in significant amount (32.3 wt%). According to Divya et al. [67], 30 wt% Ag-nanoparticles showed catalytic degradation/complex formation activity towards organic compounds (Rhodamine B), which may be the evidence of catalytic degradation/complex formation efficiency towards naproxen (organic compound) in the present case. In case of 30 wt% at an average diameter of 48.46 nm, the release rate of Ag-nanoparticles in the form of Ag^{+} depending on the pH value from the RGO surface to the solution is quite low. With increasing wt% and decreasing size, the release rate increases [69]. Hence, the presence of Ag^{+} in the acidic pH stacked on the RGO surface may increase the removal efficiency of the naproxen molecules by adsorption/complex formation. Images of multi-elemental EDS mapping of Ag-RGO are shown in Fig. 4(c), which indicates that the Ag-RGO composite is mainly composed of C, O, and Ag elements.

2. Parametric Effects on Naproxen Adsorption Capacity

2-1. Effect of pH on the Naproxen Adsorption Capacity

The adsorbate and adsorbent interaction depends on the following interactive forces: (a) electrostatic attraction or repulsion between the charged adsorbent and naproxen molecules, (b) π-π interaction (between reduced graphene oxide and the benzene ring present in the naproxen molecules), and (c) H-bonding. The electrostatic interactive force depends on the isoelectric point (the pH at which a particular molecule behaves as electrically neutral in the statistical mean) which may shift towards the higher pH values with the increasing amount of doped materials [68]. In the case of the currently synthesized material, the doping percentage of the silver nanoparticles is 32.3 or higher according to the EDS spectrum (Fig. 4(b)). Hence, the pH of the solutions plays a vital role in the adsorption mechanism. The effect of pH on the NPX removal using Ag-RGO was studied at the pH values of 2.50, 4.50, 6.50, and 8.50. The acidic and basic pHs were maintained with the addition of 1 M HCl and NaOH solutions, respectively. The removal efficiency was higher at pH 4.50 than the highly acidic (pH 2.50) and highly basic (pH 8.50) conditions (Fig. 5(a)). Such adsorption nature could result in depending on the point of zero charges (PZCs) of the graphene-based materials (pH_{pzc}~6.0, the pH value when the surface has a net zero charge) [68] and the ionization form of naproxen (pKa~4.2). Hence, at pH>4.2, ionization of NPX led to forming anions. Additionally, at pH<6, the adsorbent surface behaves as positively charged and at pH>6 the adsorbent surface behaves as negatively charged [17]. Thus, the high electrostatic interactions between the oppositely charged adsorbent surfaces and the naproxen anions ensured the high adsorption capacity and efficiency of Ag-RGO toward NPX at pH 4.50. At pH<4.2, the ionic interaction is not possible, and at pH>6, the electrostatic repulsive force between the naproxen anions and negatively charged surfaces of the adsorbent diminishes the adsorption capacity and efficiency. Moreover, with decreasing pH value, the detachment of Ag^+ from the RGO surface increases [69]. At pH 2.50, the more number of Ag^+ released into the solution decreasing the adsorption on the adsorbent surface, whereas at pH 4.50, most of the Ag^+ ions remain on the RGO surface increasing the adsorption capacity towards negatively charged naproxen anions. The maximum adsorption capacity and efficiency were obtained at pH 4.50, considered as the optimum pH value.

2-2. Effect of the Initial Naproxen Concentration on the Adsorption Capacity

The effect of initial concentration on the adsorption capacities was studied using 100 mg dm^{-3}, 50 mg dm^{-3} and 25 mg dm^{-3} NPX solutions at room temperature (298 K) for a fixed value of adsorbent dose (20.2 mg per 50 cm^3). It was observed that for particular pH value, the adsorption capacity increased with the increase of initial NPX concentration in the solution probably due to the availability of more NPX anions for adsorption before the surface vacant site saturation point reached (Fig. 5(b)). Beyond the saturation point, the adsorption capacity will remain constant even if the initial concentration increases. At the present experimental condition, 100 mg dm^{-3} showed the higher adsorption capacity of 229.25

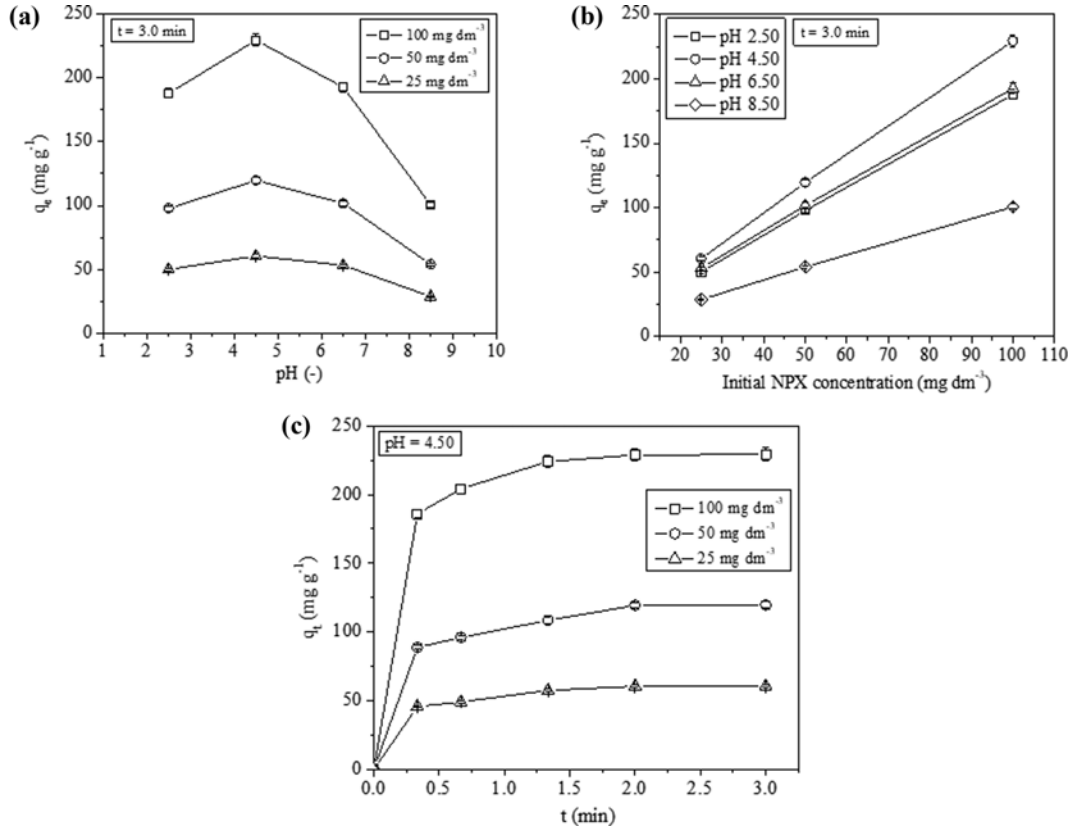

Fig. 5. Variations of the adsorption capacities depending on the (a) pH, (b) initial NPX concentration and (c) contact time.

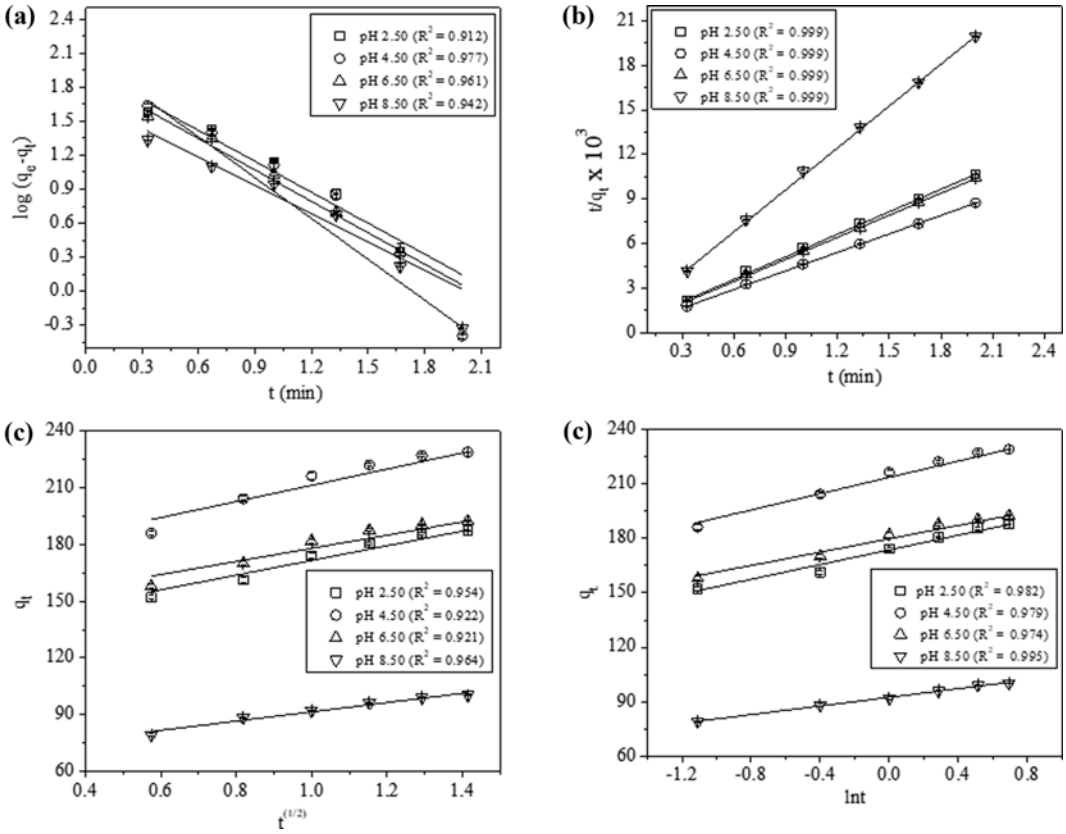

Fig. 6. NPX adsorption kinetics: (a) pseudo-first-order model, (b) pseudo-second-order model, (c) intra-particle diffusion model and (d) Elovich model.

mg g^{-1} (92.62%) at the pH 4.50.

2-3. Effect of the Contact Time on the Naproxen Adsorption Capacity

Generally, the physical adsorption capacity of the adsorbent material increases with the increase of contact time. But when ionic interactions present between surfaces of the adsorbent and the adsorbate ions, the adsorption process becomes faster. The effect of contact time on the adsorption capacities was examined by mixing 20.2 mg of Ag-RGO into 50 cm^3 aqueous solution of NPX (for the optimum pH value of 4.5 at different NPX concentrations of 25-100 mg dm^{-3}) and collecting the samples at different time intervals (Fig. 5(c)). The removal efficiency reached to 75.13% within 0.33 min and increased to 92.46% in 2.0-3.0 min for 100 mg dm^{-3} concentration at a pH value of 4.50. Which demonstrated the rapid adsorption of NPX on the adsorbent surface before reaching the equilibrium due to the possible interactions between the positively charged external surface and the negative NPX anions. The adsorption of NPX using Ag-RGO attained the equilibrium within 2.0 min to 3.0 min as the removal capacities were not changed significantly (Fig. 5(c)). Therefore, 3.0 min can be considered as the equilibrium time for further adsorption studies.

3. Adsorption Kinetics

Pseudo-first-order, pseudo-second-order, intra-particle diffusion, and Elovich models were used to estimate the kinetic parameters of the NPX adsorption at the pH 2.50-8.50, contact time 3 min, adsorbent dose 20.2 mg and initial NPX concentration of 100 mg dm^{-3} obtained from the previous optimization results (Fig. 5). The linearized form of the pseudo-first-order model can be expressed as Eq. (4) [15,17]:

$$\log(q_e - q_t) = \log q_e - \frac{k_1 t}{2.303} \tag{4}$$

where q_e and q_t are the amount of NPX adsorbed (mg g^{-1}) at equilibrium and at time t. k_1 (min^{-1}) is the first-order rate constant, which can be obtained from the log (q_e–q_t) versus t (min) plot (Fig. 6(a)). The pseudo-second-order model can be expressed by Eq. (5) [15,17]:

$$\frac{t}{q_t} = \frac{1}{k_2 q_e^2} + \frac{t}{q_e} \tag{5}$$

The intercept and slope of the plot t/q_t against t represent the values of the second-order rate constant k_2 (g mg^{-1} min^{-1}) and q_e, respectively (Fig. 6(b)). The intra-particle diffusion model is represented by Eq. (6) [2]:

$$q_t = k_p t^{1/2} + C_1 \tag{6}$$

where k_p, rate constant (mg g^{-1} $min^{-1/2}$) which can be calculated from the slope of q_t versus $t^{1/2}$ plot and C_1 is the intercept (Fig. 6(c)). This model can explain the steps of the diffusion. The Elovich model is used to demonstrate the occurrence of the chemisorption, applied for the adsorption taking place on the heterogeneous surfaces. The linearized Elovich equation is expressed by Eq. (7) [70]:

Table 1. Kinetic parameters for the NPX adsorption onto the Ag-RGO nanocomposite film (NPX concentration, 100 mg dm^{-3}; the volume of NPX solution, 50 cm^3; Ag-RGO dose, 20.2 mg; temperature, 298 K and contact time, 0.33-3 min)

Kinetic models	pH	Kinetic parameters		R^2	ARE%
Pseudo-first-order	2.50	k_1=2.096	q_e=91.80	0.912	56.12
	4.50	k_1=2.764	q_e=120.00	0.977	50.44
	6.50	k_1=2.126	q_e=79.24	0.961	63.35
	8.50	k_1=1.920	q_e=48.24	0.942	57.80
Pseudo-second-order	2.50	k_2=0.056	q_e=197.98	0.999	3.02
	4.50	k_2=0.044	q_e=237.58	0.999	3.28
	6.50	k_2=0.051	q_e=200.60	0.999	3.55
	8.50	k_2=0.086	q_e=104.54	0.999	3.10
Intra-particle diffusion	2.50	k_p=38.90	C_1=132.68	0.954	1.45
	4.50	k_p=42.83	C_1=168.55	0.922	1.63
	6.50	k_p=34.88	C_1=143.12	0.921	1.64
	8.50	k_p=24.48	C_1=66.90	0.964	1.14
Elovich	2.50	a_e=1.09×10^5	b_e=0.050	0.982	0.85
	4.50	a_e=3.08×10^5	b_e=0.045	0.979	0.82
	6.50	a_e=3.29×10^5	b_e=0.054	0.974	0.93
	8.50	a_e=0.29×10^5	b_e=0.084	0.995	0.41

$$q_t = \frac{\ln(a_e b_e)}{b_e} + \frac{1}{b_e}\ln t \quad (7)$$

where a_e and b_e represent the initial adsorption rate (mg g^{-1} min^{-1}) and the extent of the surface coverage used to analyze the chemical adsorption (g mg^{-1}) or the activation energy required for chemisorption. The values of these parameters can be acquired from the intercept and slope of the q_t versus lnt plot (Fig. 6(d)).

The average relative errors (ARE%) were estimated to ascertain the deviation between the experimental data and the data obtained from the kinetic and isotherm models by using Eq. (8).

$$\mathrm{ARE}(\%) = \frac{100}{N}\sum_{1}^{N}\left|\frac{q_{cal} - q_{exp}}{q_{exp}}\right| \quad (8)$$

where N is the number of data points. The equilibrium adsorption capacities, q_{exp} and q_{cal} (mg g^{-1}) represent the experimental and calculated values from the models. The parameters, calculated from the kinetic models, are tabulated in Table 1.

The experimental data fitted with the pseudo-second-order kinetic model with the higher correlation coefficient value of R^2=0.99 and lower ARE% compared with the pseudo-first-order kinetic model at all pH values. The minimum k_2 value (k_2=0.044) at pH 4.50 corresponds to the relatively high driving force of the concentration gradient sustained for more extended time for the adsorption of the NPX anions (NPX dissociation occurs at that pH value to form NPX anions) towards positively charged binding sites of Ag-RGO surface giving higher adsorption capacity [62,70]. The q_e value at that pH (237.58 mg g^{-1}), was only 3.63% higher than the experimental equilibrium value (229.25 mg g^{-1}) and the q_t values deviate with the low ARE% of 3.28. This tendency provides the evidence of an indication that the rate-limiting step for the adsorption of NPX on the Ag-RGO surface followed the chemisorption process involving valence forces by sharing the electrons between the adsorbent surface and the adsorbate molecules. The increasing pH value causes the negatively charged surface, and the k_2 values also increased from 0.044 to 0.086. In the case of intra-particle diffusion model, the non-zero value of intercept C_1 shown in Table 1 explains the fact that the adsorption process follows a complex mechanism not only the intra-particle diffusion as the rate-limiting step [40,71]. The higher value of k_p (k_p=42.83) at pH 4.50 validates the existence of intra-particle distribution at that pH. According to the results shown in Table 1, the a_e values of the Elovich model were high enough to satisfy the kinetic data, as demonstrated in Fig. 5, exhibiting fast adsorption kinetics where the equilibrium attained within 3 min. Moreover, the much lower values of b_e were also (smallest b_e=0.045, for pH 4.50) the evidence of excellent adsorption and effective π-π interaction between the Ag-RGO and NPX molecular surfaces [40,72]. At the pH value of 4.50, the Elovich model held a higher correlation coefficient value of R^2=0.98, and the q_t values deviate with the very low ARE% of 0.82, which was the authentication of the chemisorption process. Sample calculations of the kinetic models were represented in Table S1-S4 (supplementary material).

4. Adsorption Isotherms

Adsorption isotherms experimented at the pH range of 2.50-8.50 with the 50 cm^3 NPX solutions of different concentrations (25-100 mg dm^{-3}) for the contact time of 3 min and the adsorbent dose of 20.2 mg in each case. Langmuir, Freundlich, Temkin, and Dubinin-Radushkevich (D-R) adsorption isotherm models were studied. The Langmuir adsorption model, applicable mainly for the monolayer adsorption processes where the surfaces of the adsorbent are uniform, can be represented by the Eq. (9) [2]:

$$\frac{C_e}{q_e} = \frac{1}{bQ_m} + \frac{C_e}{Q_m} \quad (9)$$

where b (dm^3 mg^{-1}) and Q_m (mg g^{-1}) are the adsorption affinity con-

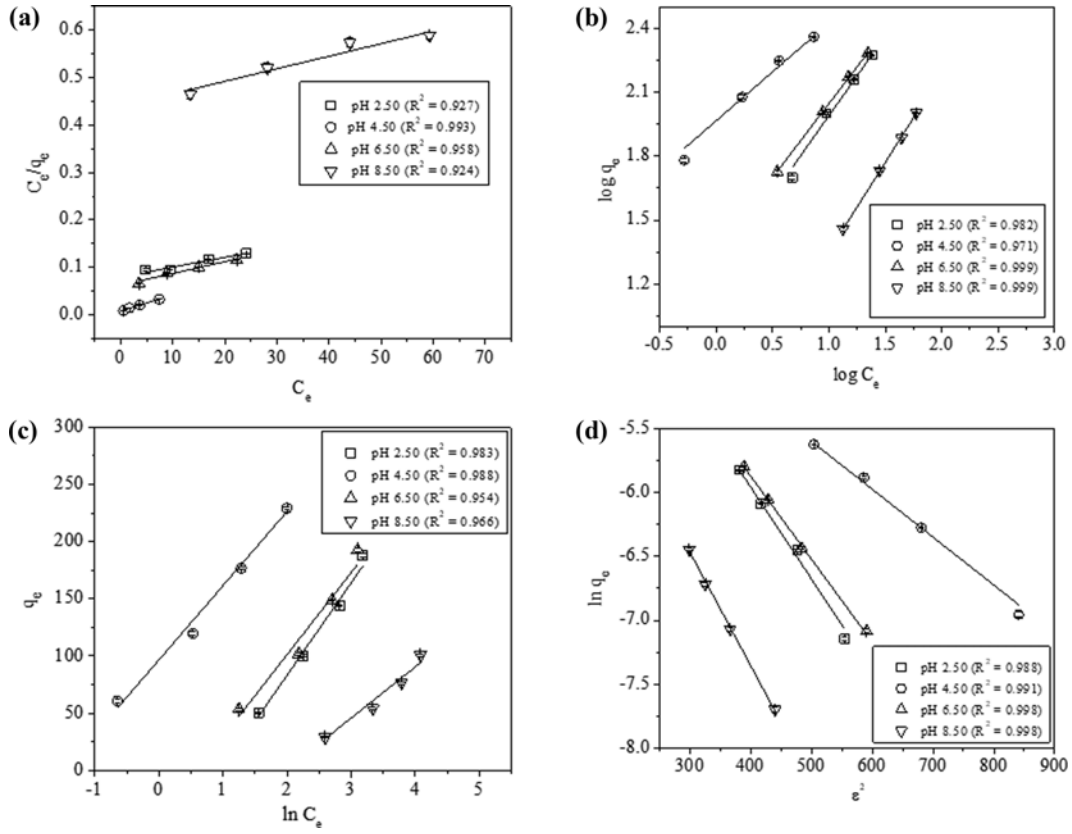

Fig. 7. Adsorption isotherms: (a) Langmuir, (b) Freundlich, (c) Temkin, and (d) Dubinin-Radushkevich (D-R).

stant at equilibrium and the maximum adsorption capacity. The coefficients were estimated from the intercept and slope of the C_e/q_e versus C_e plot (Fig. 7(a)). Freundlich isotherm which explains the adsorption on the heterogeneous surfaces is represented by Eq. (10) [2]:

$$\log q_e = \log k_f + \frac{1}{n}\log C_e \tag{10}$$

where k_f (mg g^{-1}) and n are the adsorption capacity and its intensity, which can be calculated from the intercept and slope of log q_e versus log C_e plot (Fig. 7(b)). The Temkin isotherm model characterizes the adsorbate and adsorbent interactions. The linear decrease of adsorption heat with the surface coverage of uniform energy binding sites is the primary assumption of that model. The Temkin model can be expressed by Eq. (11) [70]:

$$q_e = B\ln k_t + B\ln C_e \tag{11}$$

where k_t (is related to the equilibrium binding energy, dm^3 mg^{-1}) and B ($=\frac{RT}{b'}$, is associated with the heat of adsorption, where R is the molar gas constant (8.314×10^{-3} kJ mol^{-1} K^{-1}), T is the absolute temperature in K and b′ is the Temkin isotherm constant in kJ mol^{-1}) are the Temkin isotherm constants, can be obtained from the q_e versus lnC_e plot (Fig. 7(c)). The application of the D-R model is to examine the adsorption processes on the heterogeneous surfaces having the variable potentials of the binding sites. The D-R model is represented by Eq. (12) [17]:

$$\ln q_e = \ln q_s - B'\varepsilon^2 \tag{12}$$

where q_s and q_e are the adsorption capacity (mol g^{-1}) and equilibrium NPX concentration on the adsorbent surface (mol g^{-1}). The constants of the model, q_s and B′ (mol^2 $k J^{-2}$) can be calculated from the lnq_e versus ε^2 plot (Fig. 7(d)). ε is the Polanyi potential, related to the equilibrium concentration and expressed as follows (Eq. (13))

$$\varepsilon = RT\ln\left(1+\frac{1}{C_e}\right) \tag{13}$$

C_e is the equilibrium NPX concentration in the solution (mol dm^{-3}). The mean free energy of adsorption (E) is calculated by the Eq. (14) [17].

$$E = 1/\sqrt{2B'} \tag{14}$$

Fig. 7 represents the isotherm models, and the model constants are described in Table 2, which indicate that the adsorption pathways or the isotherm followed changed with the change in pH values. Through the correlation coefficient values were high enough, the experimental data were not satisfied by the Langmuir monolayer adsorption capacity as it showed very high deviation from the experimental data at all the pH values. Hence, the experimental data may be satisfied by the Freundlich isotherm model.

The constant k_f, which shows the tendency of the adsorbent to adsorb, ranges from 3.27 to 92.71 mg g^{-1} and n represents the potentiality of the adsorbate to be adsorbed hold the values greater than

Table 2. Adsorption isotherm constants for the sorption of NPX onto the Ag-RGO (NPX concentrations, 25, 50, 75 and 100 mg dm^{-3}; the volume of NPX solution, 50 cm^3; Ag-RGO dose, 20.2 mg; temperature, 298 K and contact time, 3 min)

Isotherms	pH	Constants			R^2	ARE%
Langmuir	2.50	Q_m=483.09	b=0.026		0.927	2.61
	4.50	Q_m=302.11	b=0.414		0.993	3.74
	6.50	Q_m=406.50	b=0.039		0.958	2.77
	8.50	Q_m=378.79	b=0.006		0.924	1.57
Freundlich	2.50	k_f=17.44	n=1.33		0.982	1.09
	4.50	k_f=92.61	n=2.18		0.971	1.16
	6.50	k_f=22.63	n=1.44		0.999	0.17
	8.50	k_f=3.27	n=1.19		0.999	0.18
Temkin	2.50	B=80.67	K_t=0.38		0.983	4.30
	4.50	B=64.84	K_t=4.43		0.988	5.63
	6.50	B=71.62	K_t=0.56		0.954	7.92
	8.50	B=44.61	K_t=0.14		0.966	7.08
D-R	2.50	q_s=0.046	B′=0.0071	E=8.39	0.988	5.74
	4.50	q_s=0.025	B′=0.0037	E=11.62	0.991	4.68
	6.50	q_s=0.036	B′=0.0064	E=8.84	0.998	3.68
	8.50	q_s=0.022	B′=0.0088	E=7.54	0.998	2.97

1 in all the cases. The highest values of k_f and n were obtained at pH 4.50, with the low ARE% of 1.16. The q_e value calculated at that pH was 231.69 mg g^{-1}, 1.06% higher than the experimental q_e value (229.25 mg g^{-1}). Therefore, the Freundlich isotherm model indicates the favorable multilayered adsorption of NPX on the heterogeneous surface of Ag-RGO nanocomposite film. The positive values of the Temkin constant B obtained in the present context designate the endothermic nature of the process, which provides evidence of chemical or ionic interaction rather than the physical adsorption [73]. The D-R isotherm model analyzed the mean free energy (E) required for the adsorption process along with the type of adsorption. According to Kose et al. [74], the free energy, E> 8 kJ mol^{-1} is responsible for the chemical adsorption process, but according to Argunet et al. [75], when 8 kJ mol^{-1}<E<16 kJ mol^{-1}, ion-exchange is the governing factor. In the case of E>16 kJ mol^{-1}, the diffusion processes mainly govern the adsorption. As shown in Table 2, the E values varied from 7.54 (at pH 8.50) to 11.62, indicating that the nature of adsorption changes from physical to chemical or ion-exchange type with the change in pH values. A good agreement with the chemical or ion-exchange route of adsorption was observed at the optimum pH value (pH=4.50), having maximum E value of 11.62 kJ mol^{-1} and minimum B' value (activation energy required for the adsorption process) of 0.0037 mol^2 kJ^{-2}. Sample calculations of the isotherm models are shown in Tables S5, S6, S7, and S8 for Langmuir, Freundlich, Temkin, and Elovich models, respectively.

The Langmuir isotherm and the pseudo-second-order kinetic model showed a higher correlation coefficient and a fixed value for NPX adsorption, which could have a close similarity with the bond formation between the NPX anions and the positively charged groups; however, the higher correlation coefficients of Freundlich isotherm recommends more than one mechanism and a degree of heterogeneity for the ionic species present in the solution and on the substrate surface. Therefore, the results obtained from the experimental data make it difficult to suggest a specific mechanism for the adsorption of NPX anions on the surfaces of Ag-RGO nanocomposite film.

5. Statistical Analysis

The user-defined discrete design and reduced quadratic model of RSM were used to optimize the following three parameters: pH (A), initial NPX concentration (B, mg dm^{-3}), and the contact time (C, min) (Table S9) to maximize the NPX adsorption capacity on the surface of Ag-RGO film. A statistical regression model equation was developed to optimize the parametric conditions of the adsorption process. The employment of the experimental process data and the variables overall interactive effects on it makes the methodology practicable. The average equilibrium adsorption data, q_e (mg g^{-1}) were used to acquire the predicted responses (Table S10). The statistical analysis utilizes experimental data, and their interactions on the process which was accomplished by placing the experimental process data to a model equation expressed as (Eq. (15)) [73,76],

$$Y = \beta_o + \sum_{j=1}^{k} \beta_j x_j + \sum_{j=1}^{k} \beta_{jj} x_j^2 + \sum\sum_{i>j} \beta_{ij} x_i x_j + e_i \quad (15)$$

where Y and β_o represent the response and a coefficient (constant); β_j, β_{jj} and β_{ij} are the linear, quadratic and second-order interaction coefficients, x_i and x_j are the independent variables; k and e_i are assigned for the number of designed factors and the error terms, respectively. The parameters are shown in Eq. (15) can be estimated by using the formula,

$$X_i = \frac{x_i - x_o}{\Delta x_i} \quad (16)$$

where x_i and x_o represent the coded and uncoded values (at the center point) of the i^{th} independent variable and Δx_i is the step

Table 3. Naproxen adsorption capacity of various kinds of adsorbents along with their fitted kinetic and isotherm models

Adsorbent used	Kinetic model	Isotherm model	pH (-) for maximum adsorption	Initial NPX concentration (mg dm^{-3})	Maximum adsorption capacity (mg g^{-1})	Reference
Activated carbon from waste apricot	Pseudo-second-order	Langmuir	5.82	100-500	106.38	Önal et al. [2]
Activated coal	-	Freundlich	6.4	1×10^{-5}-8×10^{-4}	3.5	Yu et al. [13]
Fe_3O_4-SiO_2 nanoparticles decorated GO	-	Freundlich	5.0	10-400	31.25	Nodeh et al. [17]
RGO-hydrogel	Pseudo-second-order	Langmuir	2.0	100-1000	360	Umbreen et al. [40]
Activated carbon from agricultural by-product	Pseudo-second-order	Langmuir	2.01	20	39.5	Baccar et al. [77]
Natural clay	Pseudo-second-order	Freundlich	6.0	50	37.0	Khazri et al. [78]
Activated biochar	-	Freundlich	6.5	3.30	64.5	Jung et al. [79]
Metal-organic framework MIL-101	Pseudo-second-order	Langmuir	5.0	1-20	154.0	Hasan et al. [80]
Bone char	Pseudo-first-order	Sips model (includes the features of both Langmuir and Freundlich)	7.0	50-200	3.2	Avila et al. [81]
Carbon-based magnetic adsorbents	Pseudo-second-order	Langmuir	3.0	1-30	20.75 (carbon nanotubes) 87.79 (activated carbon)	Ilbay et al. [82]
Ag-RGO	Pseudo-second-order, Elovich	Freundlich, D-R	4.50	25-50	229.25	Present study

change values between the low (−1) and high level (+1). The $\log_{10}$ transformed and reduced quadratic model equation represented in terms of the coded factors is expressed by Eq. (17).

$$\log_{10}(q_t) = +2.16 + 0.0099A + 0.2963B + 0.0597C - 0.0141BC - 0.0833A^2 - 0.0912B^2 - 0.0466C^2 \quad (17)$$

Predictions about the response can be made using Eq. (17), in terms of coded factors. The F-test in ANOVA (analysis of variance) assessed the importance of the developed equation and its virtue of fit (Table S11) and the R^2 values (Table S12). A large *F*-value (5257.40) and a low *p*-value (<0.05) validate the significance of the model and model terms. From Table S12, it is clear that the prescribed values were sufficient enough to estimate a precise response having the standard deviation (std. dev.), the coefficient of variance (CV, %), the adjusted and predicted R^2 values of 0.0069, 0.3437, 0.9993 and 0.9989, respectively. The CV value (the ratio of the stand. dev. to the mean value of response) determines the reproducibility of the model. A model is considered as sensitive if its CV value is less than 15%. The plausibility of the developed model equation was firmly established by the diagnostic plots: (a) normal probability against externally studentized residuals, (b) predicted versus actual values of adsorption capacity, and (c) externally studentized residuals versus predicted values for NPX adsorption (Fig. S1). The plots revealed that the experimental data were satisfied well by the expected data (statistical analysis data). The contemporaneous effect of time and initial NPX concentration at the pH 4.50 is shown in Fig. S2(a), which reveals that the adsorption capacity increases with the increase of initial NPX concentration and contact time due to the greater driving force at higher concentration to overcome the mass transfer limitations. The significant factors to control the adsorption capacities are the initial concentration of NPX solution and the time of contact at pH 4.50, as shown in the perturbation plot (Fig. S2(b)). The process optimization results, achieved from the design expert software, were quite similar to the experimental optimization results (Fig. 8).

The adsorption capacity obtained at the numerically optimized conditions (pH: 4.70, NPX concentration: 98.70 mg dm^{-3} and time: 2.49 min) is 233.10 mg g^{-1} (Fig. 8(a)), 1.68% higher than the value estimated at experimentally optimized conditions (229.25 mg g^{-1} at pH: 4.50, NPX concentration: 100 mg dm^{-3} and time: 3 min). When the pH was targeted to 4.50, and the other two parameters were maximized, the adsorption capacity achieved from the design expert software was 228.98 mg dm^{-3}, which was only 0.12% lower than the experimental value of 229.25 mg g^{-1} as shown in Fig. 8(b). The 3D plot for the surface response of NPX adsorption onto Ag-RGO nanocomposite film concerning the actual pH factor is represented in Fig. 9, where at the pH 4.50 and NPX concentration 100 mg dm^{-3}, the maximum adsorption capacity was obtained.

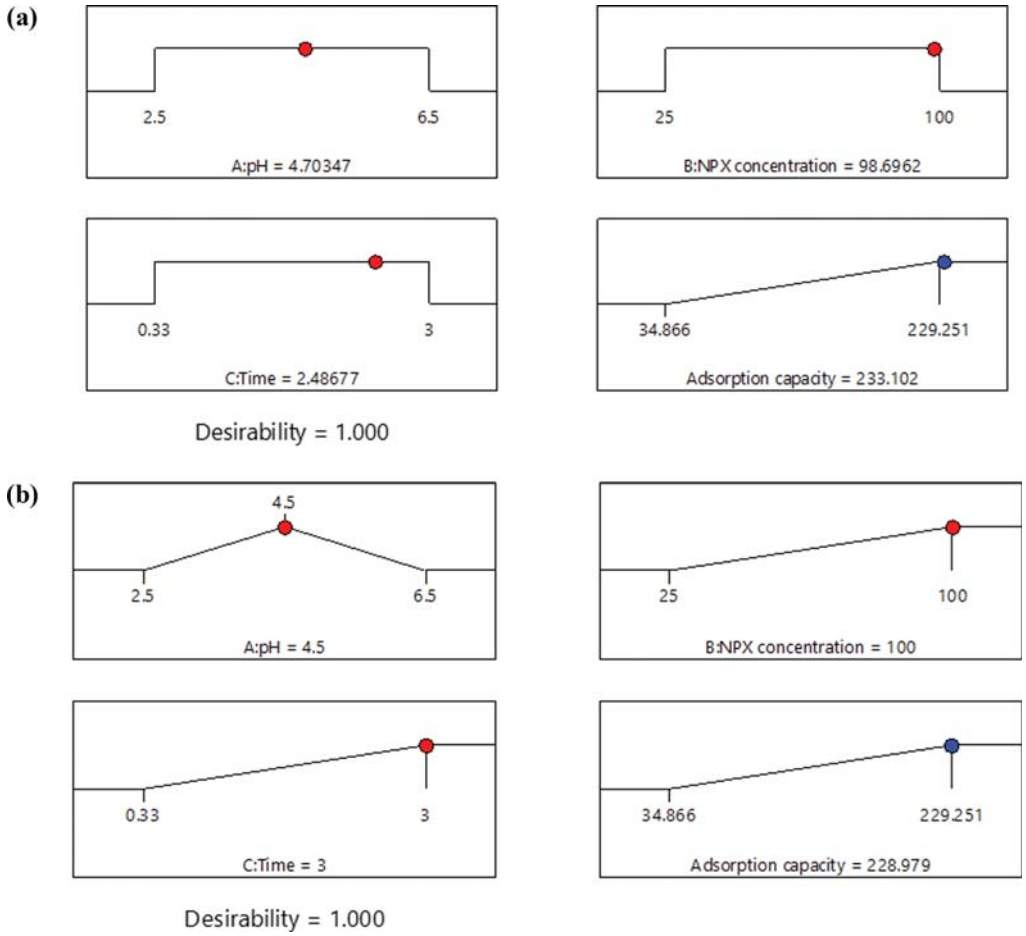

Fig. 8. Numerical optimization for the (a) independent factors varied within the range (pH, initial concentration, time) to get the maximum response (adsorption capacity) and (b) user-defined factors (pH targeted to 4.50, NPX concentration and time focused to maximum) to get maximum response.

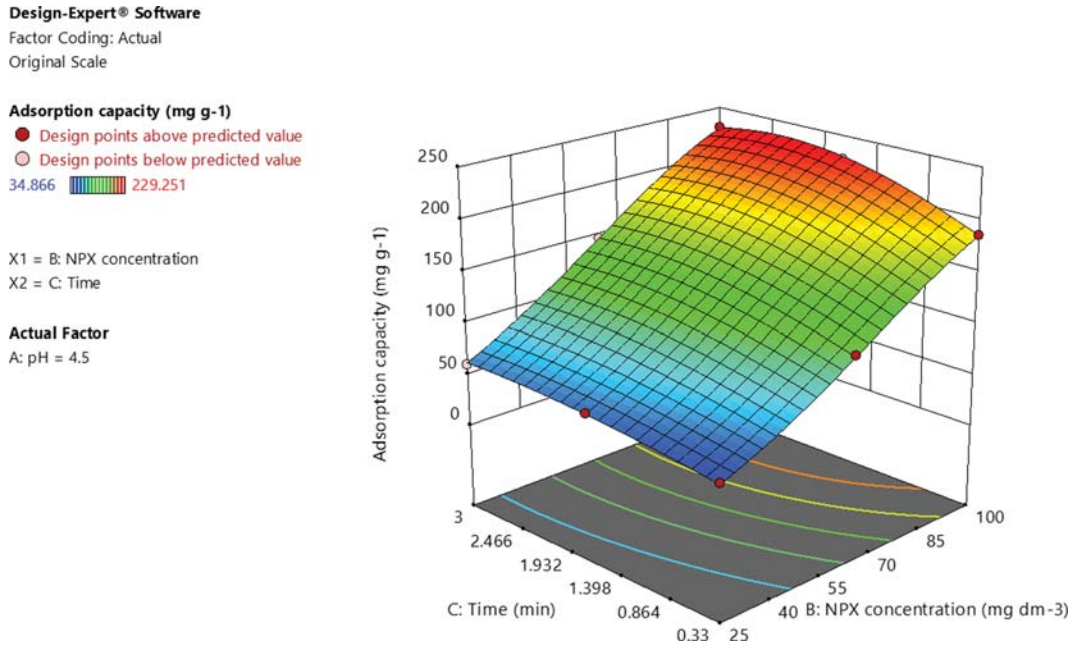

Fig. 9. 3D plot for the surface response of NPX adsorption onto Ag-RGO nanocomposite film concerning actual factor: pH=4.50.

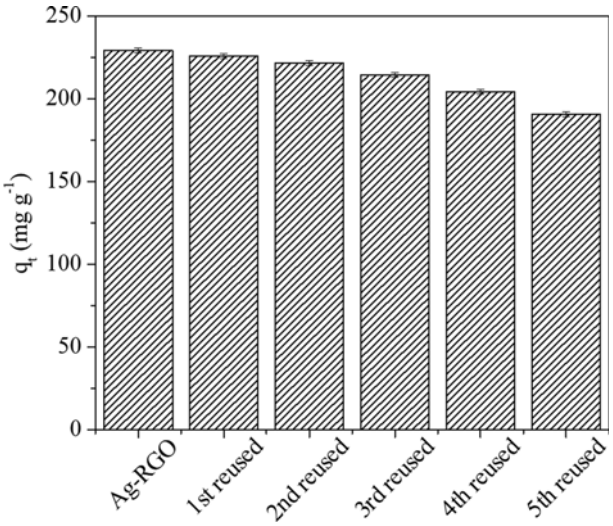

Fig. 10. Effect of recycling numbers on the adsorbed amount of NPX over Ag-RGO composite (pH: 4.50, adsorption time: 3 min and initial concentration of NPX: 100 mg dm^{-3}).

Hence, the experimental observations were satisfied by the numerical analysis data.

6. Regeneration of the Adsorbent

The samples used in the highest adsorption conditions (pH 4.50, initial NPX concentration 100 mg dm^{-3} and adsorption time 3 min) were regenerated by washing with a conventional solvent, ethyl alcohol, and reused again for the adsorptive removal of NPX. As shown in Fig. 10, the adsorption capacity of Ag-RGO towards NPX (100 mg dm^{-3}) decreased slightly with the increasing number of recycles. However, the adsorption capacity decreased only 16.78% (38.47 mg dm^{-3}) after the fifth cycle. The regeneration data demonstrated its possible application as a suitable adsorbent in commercial plants.

CONCLUSIONS

This study demonstrates that the newly synthesized Ag-RGO nanocomposite film (following a newly developed green route) provides significant removal efficiency of 92.62% for the NPX anions from their contaminated solutions. The adsorption process was highly dependent on the pH of the initial solution, and maximum removal capacity of 229.25 mg g^{-1} was obtained at pH 4.50 for the initial NPX concentration of 100 mg dm^{-3} in less than 3 min. Pseudo-second-order kinetic model, and Elovich model best fitted the experimental data, indicating chemical/ion-exchange type of adsorption at optimum pH (pH 4.50). The innovative adsorption capacities were well explained by the Freundlich isotherm rather than the Langmuir isotherm, suggesting multilayer adsorption on the heterogeneous surfaces for the naproxen removal process. The free energy (E) and the required activation energy (B′) for the D-R adsorption isotherm held highest (E=11.62 kJ mol^{-1}) and lowest (B′=0.0037) values at pH 4.50, also confirming the chemical or ion-exchange type of adsorption. The reduced quadratic model under the user-defined discrete design of RSM well explained the parametric optimization results from the experiments. Although the NPX adsorption by Ag-RGO film is encouraging, its mechanism is very complex and not precisely defined. Further studies are required to decide the exact mechanism of the adsorption process occurring in the reaction medium. Lastly, the Ag-RGO nanocomposite film, having a high NPX adsorption capacity with the fast kinetics suggests a newly synthesized, highly efficient adsorbent in the wastewater treatment industries with excellent recyclability.

ACKNOWLEDGEMENT

The authors are thankful to the Department of Science and Technology (Water Technology Initiative), Government of India, for the financial support of this work, through the Grant Number: DST/TM/WTI/2K16/20 (C)-A, dated March 3, 2017. The authors are also grateful to Analytical laboratory, Department of Chemical Engineering and Central Instrument Facility, Indian Institute of Technology Guwahati for the assistance and support to perform the necessary analysis.

CONFLICT OF INTEREST STATEMENT

The authors declare that there is no conflict of interest.

NOMENCLATURE

a_e : initial adsorption rate of Elovich equation [mg g^{-1} min^{-1}]
b : Langmuir adsorption affinity constant at equilibrium [dm^3 mg^{-1}]
b′ : Temkin isotherm constant [kJ mol^{-1}]
B : Temkin adsorption isotherm constant [related to the heat of adsorption, -]
B′ : Dubinin-Radushkevich (D-H) model constant [mol^2 kJ^{-2}]
b_e : the extent of surface coverage for chemisorption in Elovich equation [g mg^{-1}]
C_1 : intercept value of intra-particle diffusion model [-]
C_e : solution concentration at equilibrium [mg dm^{-3}]
C_0 : initial naproxen concentration [mg dm^{-3}]
C_t : concentration of NPX in the solution [mg dm^{-3}]
E : mean free energy of adsorption [kJ mol^{-1}]
k_1 : pseudo-first-order rate constant [min^{-1}]
k_2 : pseudo-second-order rate constant [g mg^{-1} min^{-1}]
k_f : Freundlich's constant [related to adsorption capacity, mg g^{-1}]
k_p : rate constant of the intra-particle diffusion model [mg g^{-1} min$^{-1/2}$]
k_t : Temkin adsorption isotherm constant [equilibrium binding energy, dm^3 mg^{-1}]
m : adsorbent dosage [g]
n : Freundlich's constant [related to adsorption intensity, -]
N : number of data points [-]
q_{cal} : equilibrium values obtained from the isotherm model [mg g^{-1}]
q_e : adsorption capacity at equilibrium [mg g^{-1} or mol g^{-1}]
q_{exp} : equilibrium values obtained from the experiment [mg g^{-1}]
Q_m : maximum adsorption capacity [mg g^{-1}]
q_s : Dubinin-Radushkevich (D-H) model constant or adsorption capacity [mol g^{-1}]

q_t : adsorption capacity at time t [mg g^{-1}]
R : universal gas constant [kJ mol^{-1} K^{-1}]
%R : naproxen removal percentage [%]
T : temperature [K]
t : time [min]
V : volume of NPX solution taken for each batch [dm^3]
ε : Polanyi potential [-]

SUPPORTING INFORMATION

Additional information as noted in the text. This information is available via the Internet at http://www.springer.com/chemistry/journal/11814.

REFERENCES

1. M. Isidori, M. Lavorgna, A. Nardelli, A. Parrella, L. Previtera and M. Rubino, *Sci. Total Environ.*, **348**, 93 (2005).
2. Y Önal, C. Akmil-Basar and C. Sarıcı-Özdemir, *J. Hazard. Mater.*, **148**, 727 (2007).
3. D. Górny, U. Guzik, K. Hupert-Kocurek and D. Wojcieszynska, *Ecotoxicol. Environ. Saf.*, **167**, 505 (2019).
4. J.-K. Im, J. Heo, L. K. Boateng, N. Her, J. R. Flora, J. Yoon, K. D. Zoh and Y. Yoon, *J. Hazard. Mater.*, **254**, 284 (2013).
5. N. Jallouli, K. Elghniji, O. Hentati, A. R. Ribeiro, A. M. T. Silva and M. Ksibi, *J. Hazard. Mater.*, **304**, 329 (2016).
6. D. Wojcieszynska, D. Domaradzka, K. Hupert-Kocurek and U. Guzik, *J. Environ. Manage.*, **145**, 157 (2014).
7. G. Boyd, S. Zhang and D. Grim, *Water Res.*, **39**, 668 (2005).
8. I. Kim, N. Yamashita and H. Tanaka, *J. Hazard. Mater.*, **166**, 1134 (2009).
9. C. Afonso-Olivares, C. Fernández-Rodríguez, R. J. Ojeda-González, Z. Sosa-Ferrera, J. J. Santana-Rodríguez and J. M. Doña Rodríguez, *J. Photochem. Photobiol. A*, **329**, 130 (2016).
10. M. Li, Z. Chen, Z. Wang and Q. Wen, *Chemosphere*, **217**, 223 (2019).
11. S. Patel, S. K. Majumder, P. Das and P. Ghosh, *J. Environ. Chem. Eng.*, **7**, 103102 (2019).
12. J. O. Straub and K. M. Stewart, *Environ. Toxicol. Chem.*, **26**, 795 (2007).
13. Z. Yu, S. Peldszus and P. M. Huck, *Water Res.*, **42**, 2873 (2008).
14. S. Begum and M. Ahmaruzzaman, *Appl. Surf. Sci.*, **449**, 780 (2018).
15. Y. Tang, X.-M. Li, Z.-C. Xu, Q.-W. Guo, C.-Y. Hong and Y.-X. Bing, *Biotechnol. Appl. Biochem.*, **61**, 333 (2013).
16. M. Qurie, M. Khamis, F. Malek, S. Nir, S. A. Bufo, J. Abbadi, L. Scrano and R. Karaman, *CLEAN-Soil, Air, Water*, **42**, 594 (2013).
17. M. K. M. Nodeh, M. Radfard, L. A. Zardari and H. R. Nodeh, *Sep. Sci. Technol.*, **53**, 2476 (2018).
18. O. G. Apul, Q. Wang, Y. Zhou and T. Karanfil, *Water Res.*, **47**, 1648 (2013).
19. J.-Z. Sun, Z.-H. Liao, R.-W. Si, G. P. Kingori, F.-X. Chang, L. Gao, Y. Shen, X. Xiao, X. Y. Wu and Y. C. Yong, *Water Sci. Technol.*, **70**, 1663 (2014).
20. Z. J. Song, W. Ran and F. Y. Wei, *Water Sci. Technol.*, **75**, 397 (2016).
21. A. A. Nafiey, A. Addad, B. Sieber, G. Chastanet, A. Barras, S. Szunerits and R. Boukherroub, *Chem. Eng. J.*, **322**, 375 (2017).
22. S. Sang, D. Li, H. Zhang, Y. Sun, A. Jian and Q. Zhang, *RSC Adv.*, **7**, 21618 (2017).
23. D. K. Padhi, T. K. Panigrahi, K. Parida, S. K. Singh and P. M. Mishra, *ACS Sustain. Chem. Eng.*, **5**, 10551 (2017).
24. K. Zhang, H. Li, X. Xu and H. Yu, *Micropor. Mesopor. Mater.*, **255**, 7 (2018).
25. L. Lin, H. Wang and P. Xu, *Chem. Eng. J.*, **310**, 389 (2017).
26. S. Fang, Z. Zhou, J. Xue, G. He and H. Chen, *Water Sci. Technol.*, **2017**, 527 (2018).
27. J. Wang, E. C. Salihi and L. Šiller, *Mater. Sci. Eng. C*, **72**, 1 (2017).
28. J. Zhang, H. Yang, G. Shen, P. Cheng, J. Zhang and S. Guo, *Chem. Comm.*, **46**, 1112 (2010).
29. S. Pei and H.-M. Cheng, *Carbon*, **50**, 3210 (2012).
30. C. K. Chua and M. Pumera, *Chem. Soc. Rev.*, **43**, 291 (2014).
31. H. Liu, T. Li, Y. Liu, G. Qin, X. Wang and T. Chen, *Nanoscale Res. Lett.*, **11**, 211, (2016).
32. Z. Bo, X. Shua, S. Mao, H. Yang, J. Qian, J. Chen, J. Yan and K. Cen, *Sci. Rep.*, **4**, 4684, (2014).
33. X. Gao, J. Jang and S. Nagase, *J. Phys. Chem. C*, **114**, 832 (2010).
34. S. Park, J. An, J. R. Potts, A. Velamakanni, S. Murali and R. S. Ruoff, *Carbon*, **49**, 3019 (2011).
35. P. Liu, Y. Huang and L. Wang, *Synth. Met.*, **167**, 25 (2013).
36. Y. Wang, Z. Shi and J. Yin, *ACS Appl. Mater. Interfaces*, **3**, 1127 (2011).
37. G. Lee and B. S. Kim, *Biotechnol. Prog.*, **30**, 463 (2014).
38. D. Suresh, P. C. Nethravathi, H. U. Nagabhushana and S. C. Sharma, *Ceram. Int.*, **41**, 4810 (2015).
39. C. M. Park, J. Heo, D. Wang and Y. Yoon, *Appl. Catal. B.*, **225**, 91 (2018).
40. N. Umbreen, S. Sohni, I. Ahmad, N. U. Khattak and K. Gul, *J. Colloid Interface Sci.*, **527**, 356 (2018).
41. S. Navalon, A. Dhakshinamoorthy, M. Alvaro and H. Garcia, *Coord. Chem. Rev.*, **312**, 99 (2016).
42. C. Wang and D. Astruc, *Prog. Mater. Sci.*, **94**, 306 (2018).
43. M. T. Tajabadi, W. J. Basirun, F. Lorestani, R. Zakaria, S. Baradaran and Y. M. Amin, *Electrochim. Acta*, **151**, 126 (2015).
44. A. H. Qustia, R. M. Mohamed and M. A. Salam, *Ceram. Int.*, **40**, 5539 (2014).
45. L. Wang, Y. Shi, T. Wang and L. Zhang, *J. Colloid Interface Sci.*, **505**, 421 (2017).
46. N. Neella, V. Gaddam, M. M. Nayak, N. S. Dinesh and K. Rajanna, *Sens. Actuators, A*, **268**, 173 (2017).
47. T. Kavinkumar and S. Manivannan, *Ceram. Int.*, **42**, 1769 (2016).
48. O. Ovsianytskyi, Y.-S. Nam, O. Tsymbalenko, P.-T. Lan, M.-W. Moon and K.-B. Lee, *Sens. Actuators, B*, **257**, 278 (2018).
49. C.-H. Deng, J.-L. Gong, P. Zhang, G.-M. Zeng, B. Song and H.-Y. Liu, *J. Colloid Interface Sci.*, **488**, 26 (2017).
50. J. Mangalam, M. Kumar, M. Sharma and M. Joshi, *Nano-Structures & Nano-Objects*, **17**, 58 (2019).
51. H. A. Salam, P. Rajiv, M. Kamaraj, P. Jagadeeswaran, S. Gunalan and R. Sivaraj, *Int. Res. J. Biol. Sci.*, **1**, 85 (2012).
52. A. R. Vilchis-Nestor, V. Sanchez-Mendieta, M. A. Camacho-López, R. M. Gómez-Espinosa, M. A. Camacho-López and J. A. Arenas-Alatorre, *Mater. Lett.*, **62**, 3103 (2008).
53. S. Martinez, I. Olmos, J. Carballo and I. Franco, *J. Food Sci. Technol.*, **45**, 773 (2010).

54. M. Moghayedi, E. K. Goharshadi, K. Ghazvini, H. Ahmadzadeh, L. Ranjbaran, R. Masoudi and R. Ludwig, *Colloids Surf. B*, **159**, 366 (2017).
55. A. Abbaszadegan, Y. Ghahramani, A. Gholami, B. Hemmateenejad, S. Dorostkar, M. Nabavizadeh and H. Sharghi, *J. Nanomater.*, **2015**, 1 (2014).
56. N. G. Bastus, F. Merkoci, J. Piella and V. Puntes, *Chem. Mater.*, **26**, 2836 (2014).
57. D. C. Marcano, D. V. Kosynkin, J. M. Berlin, A. Sinitskii, Z. Sun, A. Slesarev, L. B. Alemany, W. Lu and J. M. Tour, *ACS Nano*, **4**, 4806 (2010).
58. S. Dutta, C. Ray, S. Sarkar, M. Pradhan, Y. Negishi and T. Pal, *ACS Appl. Mater. Interfaces*, **5**, 8724 (2013).
59. S. K. Bhunia and N. R. Jana, *ACS Appl. Mater. Interfaces*, **6**, 20085 (2014).
60. W. Shao, X. Liu, H. Min, G. Dong, Q. Feng and S. Zuo, *ACS Appl. Mater. Interfaces*, **7**, 6966 (2015).
61. T. Jiao, H. Guo, Q. Zhang, Q. Peng, Y. Tang, X. Yan and B. Li, *Sci. Rep.*, **5**, 11873 (2015).
62. M. Maryami, M. Nasrollahzadeh, E. Mehdipour and S. M. Sajadi, *Int. J. Hydrogen Energy*, **41**, 21236 (2016).
63. G. Blázquez, M. A. Martín-Lara, G. Tenorio and M. Calero, *Chem. Eng. J.*, **168**, 170 (2011).
64. I. Kiran, T. Akar and S. Tunali, *Process Biochem.*, **40**, 3550 (2005).
65. N. Meng, S. Zhang, Y. Zhou, W. Nie and P. Chen, *RSC Adv.*, **5**, 70968 (2015).
66. Y. Li, H. Zhang, B. Wu and Z. Guo, *Appl. Surf. Sci.*, **425**, 194 (2017).
67. K. S. Divya, A. Chandran, V. N. Reethu and S. Mathew, *Appl. Surf. Sci.*, **444**, 811 (2018).
68. L. Zuccaro, J. Krieg, A. Desideri, K. Kern and K. Balasubramanian, *Sci. Rep.*, **5**, 1 (2015).
69. B. Molleman and T. Hiemstra, *Environ. Sci. Nano*, **4**, 1314 (2017).
70. E. Demirbas, N. Dizge, M. T. Sulak and M. Kobya, *Chem. Eng. J.*, **148**, 480 (2009).
71. S. Sohni, K. Gul, F. Ahmad, I. Ahmad, A. Khan, N. Khan and S. B. Khan, *Polym. Compos.*, **39**, 3317 (2017).
72. G. Zhao, J. Li and X. Wang, *Chem. Eng. J.*, **173**, 185 (2011).
73. E. Inam, U. J. Etim, E. G. Akpabio and S. A. Umoren, *J. Taibah Univ. Sci.*, **11**, 173 (2017).
74. T.E. Kose, H. Demiral and N. Oztürk, *Desalin. Water. Treat.*, **29**, 110 (2011).
75. M. E. Argun, S. Dursun, C. Ozdemir and M. Karatas, *J. Hazard. Mater.*, **141**, 77 (2007).
76. H. Zhang, X. Ran, X. Wu and D. Zhang, *J. Hazard. Mater.*, **188**, 261 (2011).
77. R. Baccar, M. Sarra, J. Bouzid, M. Feki and P. Blanquez, *Chem. Eng. J.*, **211-212**, 310 (2012).
78. H. Khazri, I. Ghorbel-Abid, R. Kalfat and M. Trabelsi-Ayadi, *Appl. Water Sci.*, **7**, 3031 (2016).
79. C. Jung, J. Oh and Y. Yoon, *Environ. Sci. Pollut. Res.*, **22**, 10058 (2015).
80. Z. Hasan, E. J. Choi and S. H. Jhung, *Chem. Eng. J.*, **219**, 537 (2013).
81. H. E. R. Avila, D. I. M. Castillo, A. B. Petriciolet and J. S. Albero, *J. Mol. Liq.*, **209**, 187 (2015).
82. Z. Ilbay, S. Şahin, Ö. Kerkez and Ş. S. Bayazit, *Int. J. Environ. Sci. Technol.*, **12**, 3541 (2015).
83. web ref.: Infrared spectroscopy adsorption table, chemistry, LibreTextshttps://chem.libretexts.org/Reference/Reference_Tables/Spectroscopic_Parameters/Infrared_Spectroscopy_Absorption_Table.

Supporting Information

Bio-extract assisted in-situ green synthesis of Ag-RGO nanocomposite film for enhanced naproxen removal

Somen Mondal†, Surabhi Patel, and Subrata Kumar Majumder†

Department of Chemical Engineering, Indian Institute of Technology Guwahati, Guwahati 781039, India
(*Received 2 October 2019 • accepted 19 November 2019*)

Table S1. Calculations of the pseudo-first-order kinetic model (NPX concentration, 100 mg dm^{-3}; volume of NPX solution, 50 cm^3; Ag-RGO dose, 20.2 mg; pH, 4.50; temperature, 298 K and contact time, 0.33-3 min)

q_e	q_t	t	$\log(q_e - q_t)$	Best q_e	Best k_1	q_t (calc.) (mg g^{-1})
229.25	185.96	0.33	1.64	120.00	2.76	71.80
229.25	204.17	0.67	1.40	120.00	2.76	101.16
229.25	216.27	1.00	1.11	120.00	2.76	112.43
229.25	222.11	1.33	0.85	120.00	2.76	116.96
229.25	227.11	1.67	0.33	120.00	2.76	118.81
229.25	228.85	2.00	−0.40	120.00	2.76	119.52

k_1: First-order rate constant (min^{-1}); q_e: Amount of NPX adsorbed at equilibrium (mg g^{-1}); q_t: Amount of NPX adsorbed at time t (mg g^{-1})

Table S2. Calculations of the pseudo-second-order kinetic model (NPX concentration, 100 mg dm^{-3}; volume of NPX solution, 50 cm^3; Ag-RGO dose, 20.2 mg; pH, 4.50; temperature, 298 K and contact time, 0.33-3 min)

q_e (mg g^{-1})	t (min)	q_t (mg g^{-1})	$t/q_t \times 10^3$	Best q_e	Best k_2	q_t (calc.) (mg g^{-1})
229.25	0.33	185.96	1.77	237.58	0.044	179.38
229.25	0.67	204.17	3.28	237.58	0.044	201.64
229.25	1.00	216.27	4.62	237.58	0.044	209.98
229.25	1.33	222.11	5.99	237.58	0.044	214.46
229.25	1.67	227.11	7.35	237.58	0.044	217.31
229.25	2.00	228.85	8.74	237.58	0.044	219.19

k_2: Second-order rate constant (g mg^{-1} min^{-1})

Table S3. Calculations of the intra-particle diffusion model (NPX concentration, 100 mg dm^{-3}; volume of NPX solution, 50 cm^3; Ag-RGO dose, 20.2 mg; pH, 4.50; temperature, 298 K and contact time, 0.33-3 min)

t	$t^{1/2}$	q_t	k_p	q_t (calc.) (mg g^{-1})	C value
0.33	0.57	185.96	42.83	193.15	168.55
0.67	0.82	204.17	42.83	203.61	168.55
1.00	1.00	216.27	42.83	211.38	168.55
1.33	1.15	222.11	42.83	217.94	168.55
1.67	1.29	227.11	42.83	223.90	168.55
2.00	1.41	228.85	42.83	229.12	168.55

k_p: Intra-particle diffusion model rate constant (mg g^{-1} min$^{-1/2}$) and C: Intercept of the q_t versus $t^{1/2}$ plot

Table S4. Calculations of the Elovich model (NPX concentration, 100 mg dm^{-3}; volume of NPX solution, 50 cm^3; Ag-RGO dose, 20.2 mg; pH, 4.50; temperature, 298 K and contact time, 0.33-3 min)

t	lnt	q_t	Best b_e	Best a_e	q_t (calc.) (mg g^{-1})
0.33	−1.11	185.96	0.045	3.08×10^5	188.65
0.67	−0.40	204.17	0.045	3.08×10^5	204.52
1.00	0	216.27	0.045	3.08×10^5	213.49
1.33	0.29	222.11	0.045	3.08×10^5	219.88
1.67	0.51	227.11	0.045	3.08×10^5	224.98
2.00	0.69	228.85	0.045	3.08×10^5	229.02

a_e: Initial adsorption rate (mg g^{-1} min^{-1}) and b_e: Intercept of the q_t versus lnt plot

Table S5. Calculations of the Langmuir isotherm model (50 cm^3 NPX solution, 20.2 mg Ag-RGO, pH: 4.50, temperature: 298 K and contact time: 3 min)

Initial conc. (mg dm^{-3})	Adsorption (mg dm^{-3})	c_e (mg dm^{-3})	q_e (mg g^{-1})	c_e/q_e (g dm^{-3})	Best b	Best Q_m	q_e (calc.)
25	24.58	0.42	60.83	0.007	0.45	277.78	44.51
50	48.42	1.58	119.86	0.013	0.45	277.78	115.35
75	69.88	5.12	172.97	0.030	0.45	277.78	193.80
100	92.62	7.38	229.25	0.032	0.45	277.78	213.57

C_e: Equilibrium concentration of NPX (mg dm^{-3}); q_e: The amount of NPX adsorbed (mg g^{-1}); b: The adsorption affinity constant (dm^3 mg^{-1}) and Q_m: The maximum adsorption capacity (mg g^{-1})

Table S6. Calculations of the Freundlich isotherm model (50 cm^3 NPX solution, 20.2 mg Ag-RGO, pH: 4.50, temperature: 298 K and contact time: 3 min)

c_e (mg dm^{-3})	q_e (mg g^{-1})	log(c_e)	log(q_e)	ln(C_e)	Best n	Best k_f	log(q_e) (calc.)
0.42	60.83	−0.37	1.78	−0.86	2.18	92.61	1.80
1.58	119.86	0.20	2.08	0.45	2.18	92.61	2.06
5.12	172.97	0.71	2.24	1.63	2.18	92.61	2.29
7.38	229.25	0.87	2.36	2.00	2.18	92.61	2.37

n: Freundlich's constant (related to adsorption intensity, -) and k_f: Freundlich's constant (related to adsorption capacity, mg g^{-1})

Table S7. Calculations of the Temkin isotherm model (50 cm^3 NPX solution, 20.2 mg Ag-RGO, pH: 4.50, temperature: 298 K and contact time: 3 min)

q_e	c_e (mg dm^{-3})	ln(C_e)	Best B	k_t	q_e (calc.)
60.83	0.42	−0.86	64.84	4.43	40.86
119.86	1.58	0.45	64.84	4.43	126.08
172.97	5.12	1.63	64.84	4.43	202.50
229.25	7.38	2.00	64.84	4.43	226.21

B: Temkin isotherm constant ($=\frac{RT}{b}$, is related to the heat of adsorption, where R is the molar gas constant, 8.314×10^{-3} kJ mol^{-1} K^{-1}, T is the absolute temperature, K and b is the Temkin isotherm constant in kJ mol^{-1}) and k_t: Temkin isotherm constant (related to the equilibrium binding energy, dm^3 mg^{-1})

Table S8. Calculations of the D-R isotherm model (50 cm^3 NPX solution, 20.2 mg Ag-RGO, pH: 4.50, temperature: 298 K and contact time: 3 min)

C_e (mol dm^{-3})	ε	ε^2	q_e (mol g^{-1})	ln(q_e)	Best B′	E	Best q_s	Best q_s (mg g^{-1})	q_e (calc.)
1.8×10^{-6}	32.72	1070.55	0.0003	−8.24	0.0037	11.62	0.025	1614.79	0.0003
6.8×10^{-6}	29.46	868.08	0.0005	−7.56	0.0037		0.025	1614.79	0.0005
2.2×10^{-5}	26.54	704.56	0.0008	−7.19	0.0037		0.025	1614.79	0.0009
3.2×10^{-5}	25.64	657.29	0.0010	−6.91	0.0037		0.025	1614.79	0.0010

ε: Polanyi potential ($\varepsilon = RT\ \ln\left(1+\frac{1}{C_e}\right)$); q_s: Adsorption capacity (mol g^{-1}); q_e: Concentration of NPX in equilibrium (mol g^{-1}); C_e: Solution concentration of NPX at equilibrium (mol dm^{-3}); E: Mean free energy of adsorption ($E = 1/\sqrt{2B'}$) (kJ mol^{-1}) and B′: Model constant ($mol^2\ kJ^{-2}$)

Table S9. Factors and levels of user-defined statistical experimental design for optimization of NPX adsorption by Ag-RGO

Experimental factors	Notation	Type	Actual and coded values of optimization variables		
			Low (−1)	Mean (0)	High (+1)
pH (-)	A	Discrete	2.50	4.50	6.50
NPX concentration (mg dm^{-3})	B	Discrete	25	62.5	100
Time (min)	C	Discrete	0.33	1	3

Table S10. User-defined discrete design of experiments for NPX adsorption along with response variables (Volume of adsorbate solution, 50 cm^3; adsorbent dose, 20.2 mg and temperature, 298 K)

Run	pH (-)	NPX concentration (mg dm^{-3})	Time (min)	Response variable for adsorption capacity (mg g^{-1})
1	6.5	62.5	0.33	94.25
2	4.5	100	0.33	185.96
3	2.5	100	0.33	151.99
4	2.5	62.5	0.33	88.79
5	6.5	62.5	1.665	120.84
6	2.5	62.5	3	120.46
7	6.5	100	0.33	157.79
8	4.5	25	0.33	45.57
9	6.5	62.5	3	124.69
10	6.5	100	1.665	190.15
11	4.5	62.5	0.33	113.30
12	4.5	25	3	60.58
13	6.5	25	1.665	50.49
14	6.5	100	3	192.48
15	6.5	25	3	53.26
16	2.5	25	0.33	34.87
17	2.5	25	1.665	47.71
18	6.5	25	0.33	37.16
19	4.5	100	3	229.25
20	2.5	62.5	1.665	115.90
21	4.5	62.5	1.665	142.47
22	2.5	25	3	50.14
23	2.5	100	3	187.77
24	4.5	25	1.665	59.15
25	2.5	100	1.665	184.24
26	4.5	62.5	3	147.18
27	4.5	100	1.665	226.68

Table S11. Analysis of variance (ANOVA) for the reduced response surface quadratic model fitted to user-defined experimental design (NPX adsorption)

Source	Sum of squares	Degrees of freedom	Mean square	F-value	p-Value	
Model	1.75	7	0.2505	5257.40	<0.0001	Significant
A-pH	0.0018	1	0.0018	37.04	<0.0001	
B-NPX concentration	1.58	1	1.58	33174.80	<0.0001	
C-Time	0.0641	1	0.0641	1346.27	<0.0001	
BC	0.0024	1	0.0024	49.83	<0.0001	
A^2	0.0416	1	0.0416	873.38	<0.0001	
B^2	0.0499	1	0.0499	1047.46	<0.0001	
C^2	0.013	1	0.013	272.99	<0.0001	
Residual	0.0009	19	0			
Cor. total	1.75	26				

Table S12. The fit summary for the reduced quadratic model (Transform: Base 10 Log)

Model statistics						
Std. Dev.	Mean	C.V. (%)	R^2	Adj. R^2	Pred. R^2	Adeq. precision
0.0069	2.01	0.3437	0.9995	0.9993	0.9989	214.56

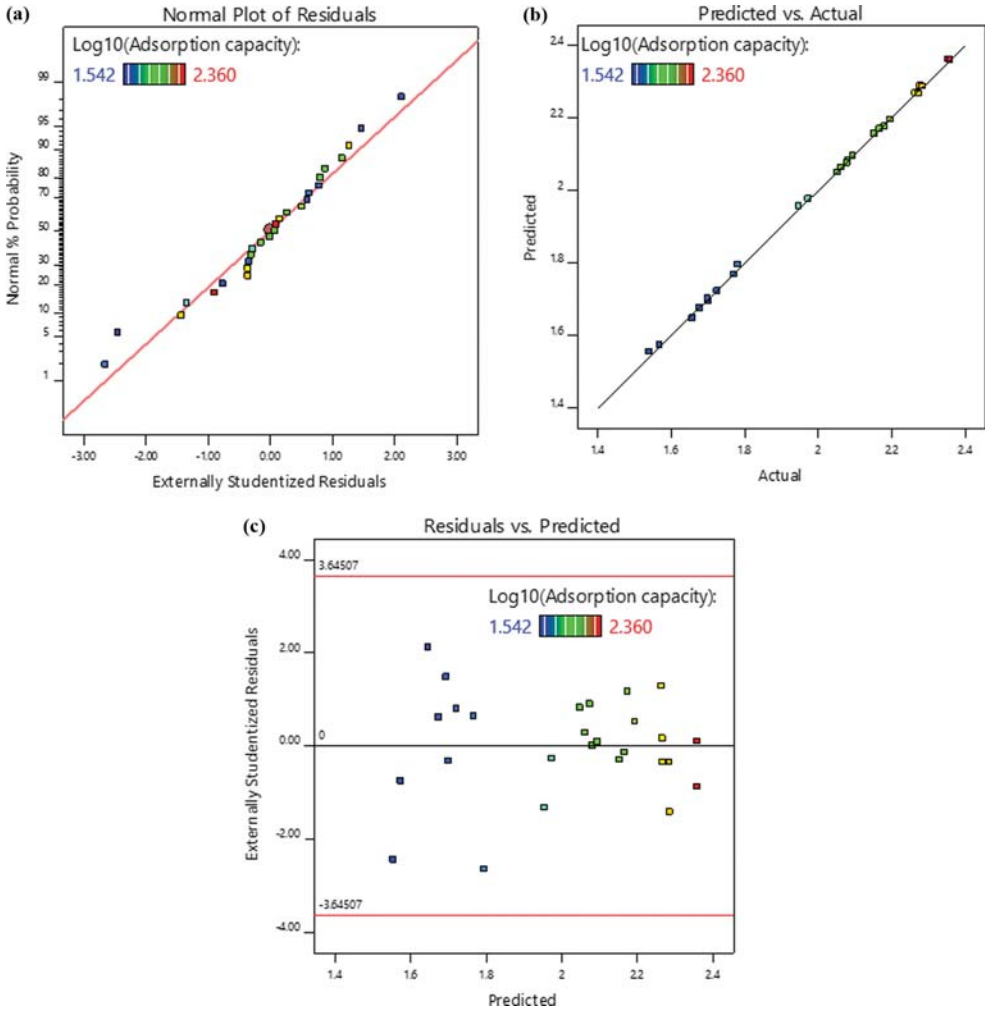

Fig. S1. (a) Normal probability against externally studentized residuals, (b) predicted versus actual values of adsorption capacity and (c) externally studentized residuals versus predicted values for NPX adsorption.

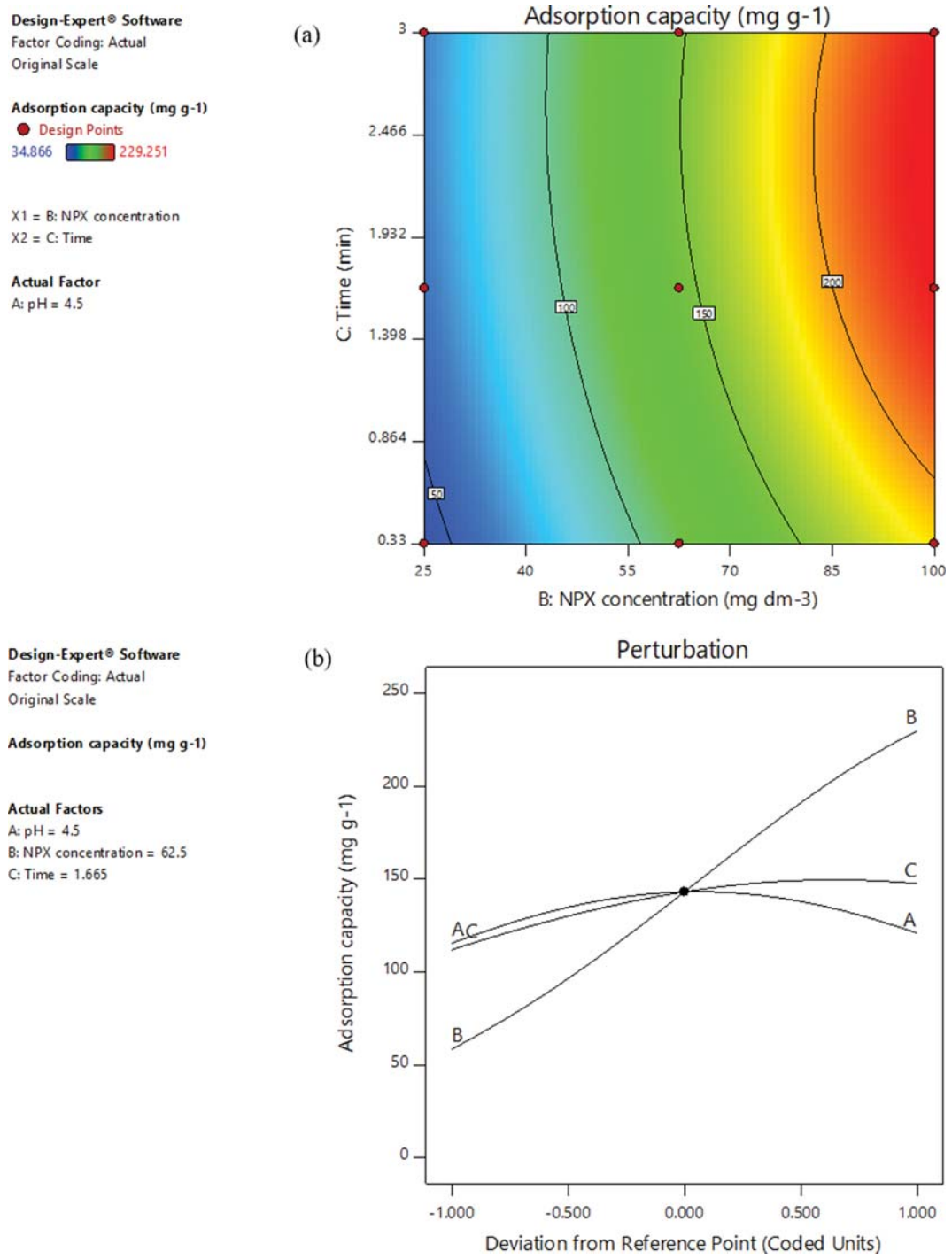

Fig. S2. (a) Contour plot showing the effect of combined factors time and NPX concentration on the adsorption capacity at pH 4.50 and (b) perturbation plot showing the impact of individual factors at the medium level.